Ore Geology Reviews 101 (2018) 765–784

Contents lists available at ScienceDirect

Ore Geology Reviews

journal homepage: www.elsevier.com/locate/oregeorev

Magmatic-hydrothermal evolution of the Yuanzhuding porphyry Cu-Mo deposit, South China: Insights from mica and quartz geochemistry

Wei Mao[a], Hong Zhong[a,b,*], Wei-Guang Zhu[a], Xiu-Guang Lin[c], Xiao-Yu Zhao[a,b]

[a] State Key Laboratory of Ore Deposit Geochemistry, Institute of Geochemistry, Chinese Academy of Sciences, 99 West Lincheng Road 550081, Guiyang, China
[b] University of Chinese Academy of Sciences, Beijing 100049, China
[c] Geological Team 719, Guangdong Bureau of Geological Exploration, Zhaoqing 526020, China

ARTICLE INFO

Keywords:
Porphyry deposit
Biotite composition
Quartz trace element
Fluid inclusion
Metal precipitation
South China

ABSTRACT

The Yuanzhuding porphyry Cu-Mo deposit, located in the southern section of the Qinzhou-Hangzhou belt, is characterized by successive generations of quartz-bearing veins with complicated crosscutting relationships. Multiple analytical methods have been applied to different mica types and quartz-bearing veins to reveal the evolution history of the Yuanzhuding porphyry system.

Four types of micas have been identified in the Yuanzhuding porphyry Cu-Mo deposit, including magmatic biotite (Bt-I), metamorphic biotite (Bt-II), hydrothermal biotite (Bt-III), and hydrothermal sericite (Ser), based on detailed petrological observations. All three types of biotite belong to the Mg-biotite group but can be compositionally distinguished, whereas Ser lies in the transition zone between Li-phengite and Li-muscovite. Generally decreasing crystallization temperatures with increasing distances from the center of the porphyry have been revealed in Bt-II and Bt-III based on their compositional variations, documenting the outward cooling trends of the Yuanzhuding porphyry system.

Early quartz-bearing veins with potassic alteration are characterized by granular quartz with homogeneous CL textures, in combination with their wavy vein walls which indicate the host rock was ductile during vein formation, we infer that they were formed under dominantly lithostatic pressure. Late quartz-bearing veins with sericitic alteration are typically euhedral quartz with growth zones of oscillating CL intensity, and they are inferred to be formed under dominantly hydrostatic pressure. Intersection of fluid inclusion isochores with Ti-in-quartz isopleths revealed that early quartz veins with potassic alteration located close to the ore-forming porphyry were formed at up to ~575 °C. Late quartz veins with sericitic alteration were formed at ~310 °C.

Formation depth of the Yuanzhuding porphyry deposit is inferred to be ~5.3 km. Hydrogen and oxygen isotopes of Bt-III and quartz indicate that the ore-forming fluid was mainly magmatic fluid. The fluid pressure was high enough to remain stable in single phase through the entire fluid evolution history. All fluid inclusions are vapor-liquid inclusions. The fluid salinity and the Cl fugacity remained constantly low, which may have limited the efficiency of Cu extraction and transportation.

The hornfels host significant amounts of Bt-II and may have served as a reservoir of ferrous iron to reduce the oxidized ore-forming fluid and generate reduced sulfur. Effective metal precipitation occurred in the Yuanzhuding porphyry system owing to the coexistence of the generation of reduced S^{2-} and the drop of metal solubility caused by the decrease of fluid temperature.

1. Introduction

Micas are one group of the most important OH-bearing minerals on Earth and are widespread in igneous, metamorphic, sedimentary rocks, and hydrothermal systems (Beane, 1974; Rieder et al., 1998; Tischendorf et al., 2007). The simplified formula of micas can be written as $IM_{2-3}\square_{1-0}T_4O_{10}A_2$, where I is commonly Cs, K, Na, NH_4, Rb, Ba, and Ca; M is commonly Li, Fe (di- or trivalent), Mg, Mn (di- or trivalent), Zn, Al, Cr, V, and Ti; □ is vacancy; T is commonly Be, Al, B, Fe (trivalent), and Si; A is commonly Cl, F, OH, and O (oxy micas) (Rieder et al., 1998). The large compositional diversity of micas makes them a potential indicator mineral from which complicated geological

* Corresponding author at: State Key Laboratory of Ore Deposit Geochemistry, Institute of Geochemistry, Chinese Academy of Sciences, 99 West Lincheng Road 550081, Guiyang, China.
E-mail address: zhonghong@vip.gyig.ac.cn (H. Zhong).

https://doi.org/10.1016/j.oregeorev.2018.08.016
Received 28 April 2018; Received in revised form 21 June 2018; Accepted 13 August 2018
Available online 16 August 2018
0169-1368/

processes in different environment can be revealed.

In contrast, quartz is one of the purest minerals in the Earth crust, ideally consisting of interconnected chains of $(SiO_4)^{4-}$ tetrahedrons extending along the crystallographic c-axis. Only a small number of ions can substitute for Si^{4+} in quartz because of the small ionic radius and high valence of Si^{4+} (Götze, 2009). As the elasticity of the crystal lattice is controlled by temperature and pressure, incorporation of trace elements in quartz is therefore controlled by the crystal-forming conditions (Jacamon and Larsen, 2009; Thomas et al., 2010). Titanium concentration in quartz was originally tested to be a geothermometer by Ostapenko et al. (2007), and further development of this tool has been carried out recently (Wark and Watson, 2006; Ostapenko et al., 2007; Thomas et al., 2010; Huang and Audétat, 2012).

Numerous studies have focused on revealing the magmatic-hydrothermal evolution of porphyry systems by gangue mineral geochemistry (e.g., Dilles and Einaudi, 1992; Wilkinson et al., 2015; Maydagán et al., 2018). For example, compositional differences between magmatic, re-equilibrated, and hydrothermal biotite have been well documented in the Darreh-Zar porphyry Cu deposit (Parsapoor et al., 2015). Ti-substitution and Mg/Fe ratio in biotite can be used for the temperature estimation of biotite crystallization (Wones and Eugster 1965; Beane 1974; Henry 2005; Nachit et al., 2005; Parsapoor et al., 2015). Equally, halogen elements in biotite can be used to estimate the fluorine and chlorine fugacities in the coexisting fluid (Munoz, 1984, 1992; Zhu and Sverjensky, 1991, 1992; Coulson et al., 2001). A detailed evaluation of the halogen fugacities of hydrothermal fluids has been conducted in many porphyry systems (Lanier et al., 1978; Parry et al., 1978; Jacobs and Parry, 1979; Taylor, 1983; Bowman et al., 1987; Loferski and Ayuso, 1995; Sheets et al., 1996; Selby and Nesbitt, 2000; Ayati et al., 2008; Boomeri et al., 2009, 2010; Afshooni et al., 2013; Parsapoor et al., 2015; Bao et al., 2016). Quartz CL textures and trace elements have been applied to reveal the complicated history of the hydrothermal fluid evolutions in many porphyry deposits (Penniston-Dorland, 2001; Rusk and Reed, 2002; Landtwing and Pettke, 2005; Mülleret al., 2010; Maydagán et al., 2015; Mao et al., 2017).

South China is one of the most important metallogenic provinces in China, with significant amounts of Mesozoic ore deposits distributed along the Qinzhou-Hangzhou Metallogenic belt (Mao et al., 2013a,b). The Yuanzhuding porphyry Cu-Mo deposit is the largest porphyry-type deposit in the southern section of the Qinzhou-Hangzhou belt (Zhong et al., 2010; Lin et al., 2011; Zhou et al., 2012; Chu, 2013; Zhong et al., 2013; Liang et al., 2015). We have integrated multiple analytical methods to demonstrate the geochemistry of different mica types and quartz-bearing veins hosted in the Yuanzhuding deposit. The results revealed the magmatic-metamorphic-hydrothermal evolution history and the ore-forming processes of the Yuanzhuding porphyry Cu-Mo system.

2. Geological setting

2.1. Regional geologic setting

South China hosts significant amounts of W-Sn-Mo-Bi-Cu-Pb-Zn-Au-Ag ore deposits formed in the Mesozoic (Hua and Mao, 1999; Mao et al., 2008, 2011a; Zhou et al., 2012). A series of porphyry-skarn Cu-(Au-Mo) deposits and related epithermal Pb-Zn-Ag deposits were formed along the NE-trending Qinzhou-Hangzhou belt in the Jurassic, including the Dexing porphyry Cu-Au-Mo deposit, Yinshan epithermal Cu-Ag-Pb-Zn deposit, Qibaoshan skarn Cu deposit, Shuikoushan Pb-Zn deposit, Baoshan porphyry Cu and hydrothermal Pb-Zn deposit, Tongshanling porphyry-skarn Cu deposit, Dabaoshan polymetallic deposit, and Yuanzhuding porphyry Cu-Mo deposit (Mao et al., 2011a, b, 2014; Liang et al., 2012, 2015; Zhou et al., 2012; Li et al., 2013), with a generally decreasing mineralization age from ~175 Ma in the northeast to ~156 Ma in the southwest (Mao et al., 2004, 2011a; Zhong et al., 2010; Wang et al., 2011a,b; Li et al., 2013; Mao et al., 2013a,b, 2017) (Fig. 1a).

Tectonic trigger for the extensive Jurassic mineralization in South China has been inferred to be the subduction of the Izanagi plate beneath the East China block (Li et al., 2008; Mao et al., 2008), although the direction of the subduction is still under debate (Zhou et al., 2006; Wang et al., 2011a,b). The ore-forming igneous rocks are all high-K calc-alkaline granites with high Sr/Y signatures (Mao et al., 2009). Variety of the country rocks has led to the various mineralization types from porphyry-type deposits to skarn and manto-type deposits (Mao et al., 2009). For example, porphyry-type mineralization was formed in the contact zone between the granitic porphyries and the meta-sedimentary tuff of the Mesoproterozoic Shuangqiaoshan Group in the Dexing area (Li et al., 2013). In contrast, the skarn-type and manto-type mineralization were formed when the granitic porphyries intruded in the carbonate country rocks in the Dabaoshan district (Wang, 2010; Mao et al., 2017).

2.2. Ore deposit geology

The Yuanzhuding porphyry Cu-Mo deposit lies 13 km northwest of the Nanfeng Town, Zhaoqing City, Guangdong Province (Fig. 1). The Upper Cambrian Shuikou Group hosts the major sedimentary rocks in the Yuanzhuding district (Fig. 2), and is mainly composed of quartzose, feldspathic or quartzofeldspathic metagreywacke, meta-sandstone, meta-siltstone, and sericite-bearing clayey shale (Zhong et al., 2010; Lin et al., 2011). The Upper Cambrian Shuikou Group was folded to form the East-West striking Yuanzhuding Anticline, with the strata dipping to the North and South at 40°~70°, respectively (Fig. 2).

The Yuanzhuding granite porphyry intruded in the fold axis of the Yuanzhuding Anticline (Figs. 2, 3). Two outcrops of the porphyry make up a total area of 0.193 km^2, with one exposed area of 0.164 km^2 and the other of 0.029 km^2. Zircon U-Pb dating yielded an emplacement age of 157.8 ± 1.1 Ma (Zhong et al., 2013). Based on the zircon U-Pb dating and Sr-Nd-Hf isotopic compositions of the ore-forming porphyry, Zhong et al. (2013) inferred that the Yuanzhuding granite porphyry was emplaced in a continental arc setting related to the westward subduction of the Paleo-Pacific plate.

The Yuanzhuding granite porphyry consists of 40~50% phenocrysts with grain size of 1~2 mm, including quartz (~35%), K-feldspar (~25%), plagioclase (~30%), and biotite (~10%). The fine-grained matrix is composed of ~55% of quartz, ~40% of feldspar, and < 5% of biotite, with grain sizes of < 0.1 mm. The quartz phenocrysts are all anhedral, with local secondary growth related to hydrothermal fluid events. K-feldspar, plagioclase, and biotite phenocrysts display subhedral to euhedral crystal shapes, and were partly to fully altered to sericite, clay minerals, calcite and dolomite (Figs. 4, 5, 6). Contact metamorphism occurred within ~400 m from the boundary of the Yuanzhuding granite porphyry. The Upper Cambrian Shuikou Group sedimentary rocks have been metamorphosed to hornfels. Abundant preexisting clay minerals have been recrystallized to biotite (Figs. 4, 5).

Hydrothermal alterations display typical zoning pattern, ranging from least altered granite porphyry in the center (partly overprinted by sericitic alteration) to potassic alteration in the contact zone between the porphyry and the host rock to sericitic alteration distal from the porphyry (Fig. 3). The Yuanzhuding porphyry Cu-Mo deposit hosts 0.98 Mt Cu with an average grade of 0.17% and 0.26 Mt Mo with an average grade of 0.045% (Chu, 2013). The Cu-Mo ore bodies are mainly distributed in the Upper Cambrian Shuikou Group close to the Yuanzhuding granite porphyry and shows concentric zonation, ranging from a Mo mineralization zone through to a Mo-Cu mineralization zone to a Cu mineralization zone with increasing distance from the granite porphyry (Figs. 2, 3). Ore minerals are mainly molybdenite, chalcopyrite, pyrite, and minor bornite and tetrahedrite. Gangue minerals include quartz, K-feldspar, biotite, sericite, clay minerals, calcite, and dolomite (Figs. 4, 5, 6). Molybdenite Re-Os dating yielded a mineralization age of 157.3 ± 4.3 Ma (Zhong et al., 2010), consistent with the formation age

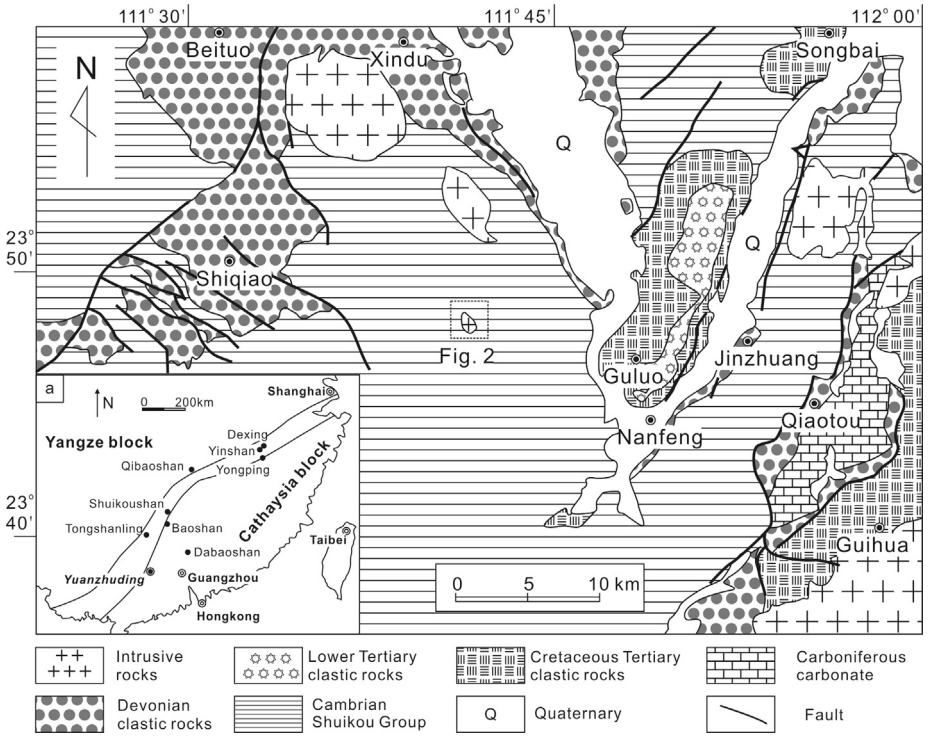

Fig. 1. Regional geological map of the study area with the location of the Yuanzhuding porphyry Cu-Mo deposit (Modified after Zhong et al., 2010).

of the Yuanzhuding granite porphyry.

Copper and molybdenite mineralization both occurred in the potassic alteration stage and the sericitic alteration stage. Chalcopyrite related to potassic alteration shows close spatial relationship with the altered primary magmatic biotite (Fig. 4.1a, b), or is hosted in the quartz-K-feldspar veins (Fig. 4.2c, d), or is disseminated in the hornfels with grain sizes of < 50 μm (Fig. 4.1e, f). Molybdenite related to potassic alteration is mainly hosted in quartz-molybdenite veins (Fig. 4.2g, h), and minor molybdenite is disseminated in the granite porphyry and the hornfels. Sericitic alteration related molybdenite mineralization is mostly hosted in the quartz-sericite-molybdenite-chalcopyrite veins (Fig. 4.2i). Significant chalcopyrite mineralization is disseminated in the sericiticly altered hornfels with grain sizes of < 50 um (Fig. 4.2j, k, l).

3. Samples and analytical methods

3.1. Samples

All samples were collected from drill holes as illustrated in Figs. 2 and 3. Drill holes ZK0-112 and ZK11-112 are mainly distributed in the potassic alteration zone. Drill holes ZK15-104 and ZK22-106 are situated in the transitional zone from potassic to sericitic alteration zone. Drill hole ZK26-100 is in the sericitic alteration zone. Petrographic

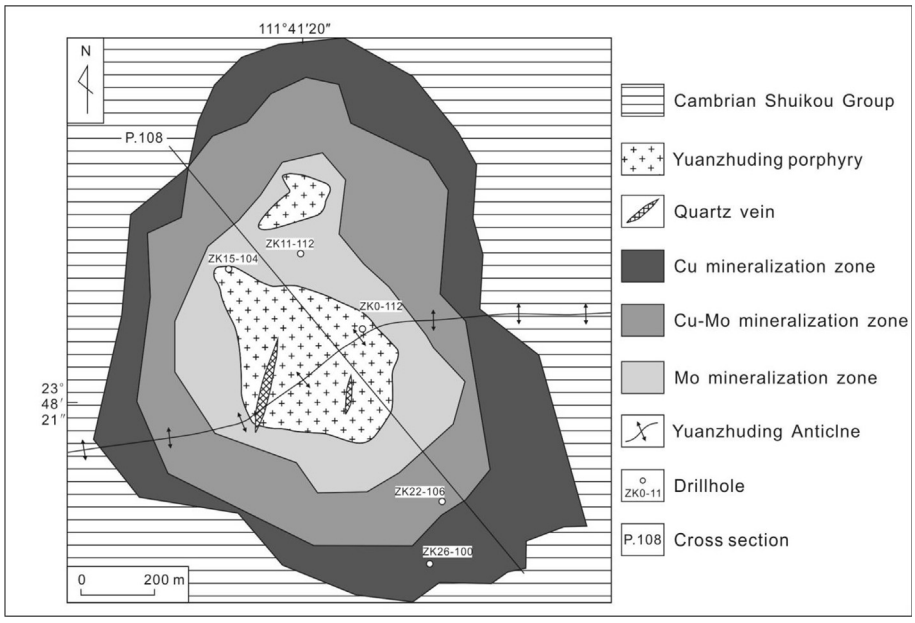

Fig. 2. Geological map of the Yuanzhuding porphyry Cu-Mo deposit (Modified after Zhong et al., 2010).

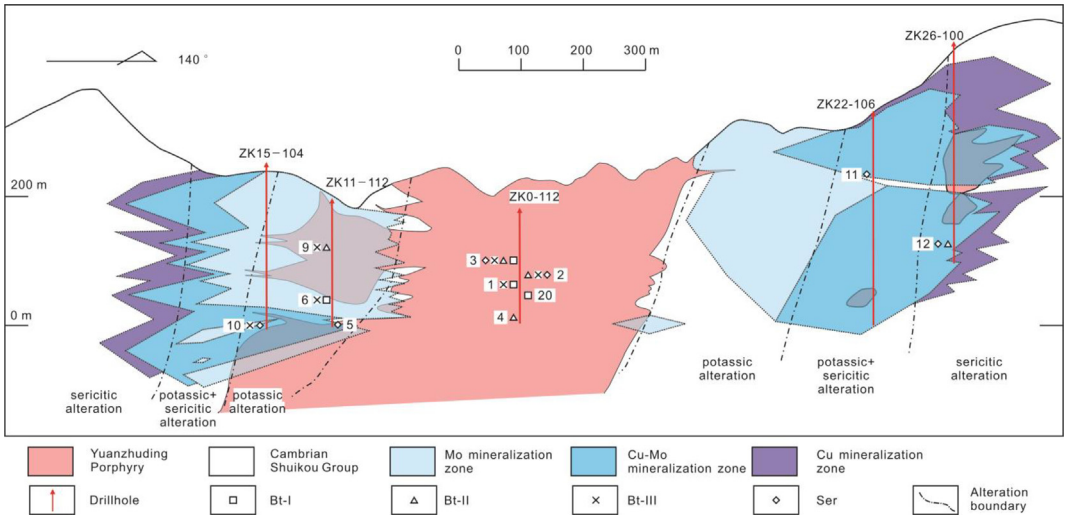

Fig. 3. Geologic cross section P. 108 of the Yuanzhuding porphyry Cu-Mo deposit, with spatial distribution of selected samples. See location of P. 108 in Fig. 2 (Modified after Chu, 2013). See sample numbers in Table 1.

study was conducted in over 40 doubly polished thin sections with the optical microscope, and 12 of them were selected for further analysis.

Samples hosting magmatic biotite (Bt-I) are from drill holes ZK0-112 (NO. 1, 3, 20 in Fig. 3) and ZK11-112 (NO. 6). Samples containing metamorphic biotite (Bt-II) are from drill holes ZK0-112 (NO. 2, 3, 4), ZK11-112 (NO. 9), and ZK26-100 (NO. 12). Samples hosting hydrothermal biotite (Bt-III) are from drill holes ZK0-112 (NO. 1, 2, 3), ZK11-112 (NO. 6, 9), and ZK15-104 (NO. 10). Samples containing hydrothermal sericite (Ser) are from drill holes ZK0-112 (NO. 2, 3), ZK11-112 (NO. 5), ZK22-106 (NO. 11), and ZK26-100 (NO. 12).

Sample ZK0-112-03 (NO. 2 in Fig. 3): This sample was hosted in the hornfels several centimeters away from the Yuanzhuding granite porphyry and is characterized by potassic alteration. The hornfels contain abundant metamorphic biotite (Fig. 5.2r). It hosts multiple quartz-bearing veins with wavy vein walls (Fig. 5.1e, f). The veins thickness varies from ~1 cm to < 0.2 mm. K-feldspar is developed along the vein edge. Hydrothermal biotite occurs in the quartz-bearing veins and was partly altered to sericite. Chalcopyrite and molybdenite are disseminated in both the hornfels and the quartz-bearing veins.

Sample ZK15-104-04 (NO. 10 in Fig. 3): This sample is situated in the hornfels several tens of meters away from the Yuanzhuding granite porphyry and is characterized by sericitic alteration. The hornfels host abundant metamorphic biotite. A quartz-sericite-molybdenite-chalcopyrite vein is developed and cut two preexisting veins. Vein walls are straight and stable at ~2 cm. Relic hydrothermal biotite have been identified in the earlier veins.

3.2. Analytical methods

3.2.1. EMPA

Compositional analyses of micas were conducted with a JOEL JXA 8230 wavelength dispersive electron microprobe at the School of Resources and Environmental Engineering, Hefei University of Technology, China. The analytical conditions were set at an accelerating voltage of 15 kV, a beam current of 20nA, an electron beam size of 3–5 μm, and counting time of 10–20 s. Natural and synthetic minerals

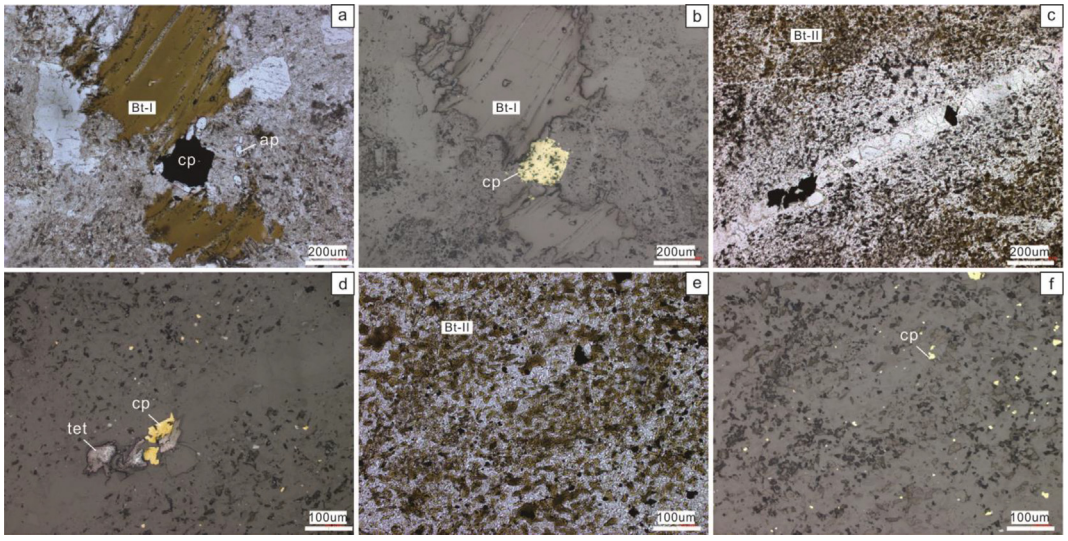

Fig. 4.1. Copper and molybdenum mineralization in the Yuanzhuding porphyry Cu-Mo deposit. (a, b) Transmitted and reflected light images of chalcopyrite mineralization related to potassic alteration hosted in the granite porphyry. (c, d) Transmitted and reflected light images of chalcopyrite mineralization related to quartz-K-feldspar vein. The dark hornfels was bleached during the potassic alteration to form an alteration halo abundant in K-feldspar. (e, f) Transmitted and reflected light images of chalcopyrite mineralization related to potassic alteration hosted in the hornfels as disseminated sulfides. ap = apatite, cp = chalcopyrite, tet = tetrahedrite, mb = molybdenite, py = pyrite, qz = quartz.

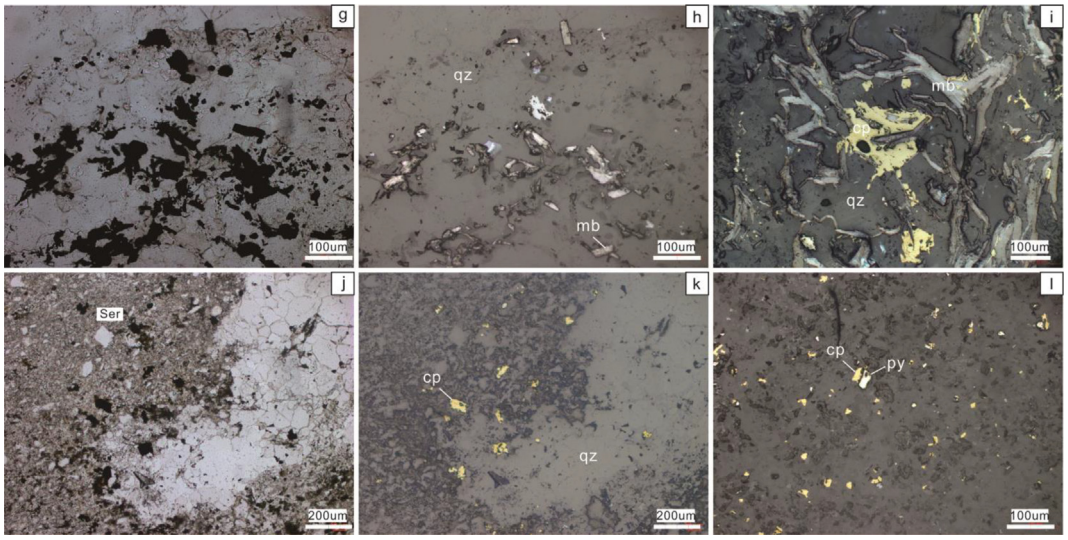

Fig. 4.2. Copper and molybdenum mineralization in the Yuanzhuding porphyry Cu-Mo deposit. (g, h) Transmitted and reflected light images of molybdenite mineralization related to potassic alteration hosted in quartz-bearing veins. (i) Chalcopyrite and molybdenite mineralization hosted in the quartz-sericite-molybdenite-chalcopyrite vein. (j, k, l) Transmitted and reflected light images of chalcopyrite mineralization hosted in the sericiticly altered hornfels. ap = apatite, cp = chalcopyrite, tet = tetrahedrite, mb = molybdenite, py = pyrite, qz = quartz.

were applied as standards, and the ZAF program was employed for matrix corrections. Mica formulas were calculated with the computer program MICA+ (Yavuz, 2003). The calculated cations were then shared into the I, M, T, and A crystallographic sites.

3.2.2. SEM-CL

SEM-CL analyses of quartz were acquired on a JSM-7800F SEM equipped with a Mono CL4 detector at the State Key Laboratory of Ore Deposit Geochemistry (SKLODG), Chinese Academy of Sciences. The acceleration voltage was set at 15 kV and the probe current was ~10nA. SEM-CL images and transmitted light images were combined to identify quartz textures and to avoid the accidental ablation of fluid and mineral inclusions in quartz during the subsequent LA ICP-MS analysis.

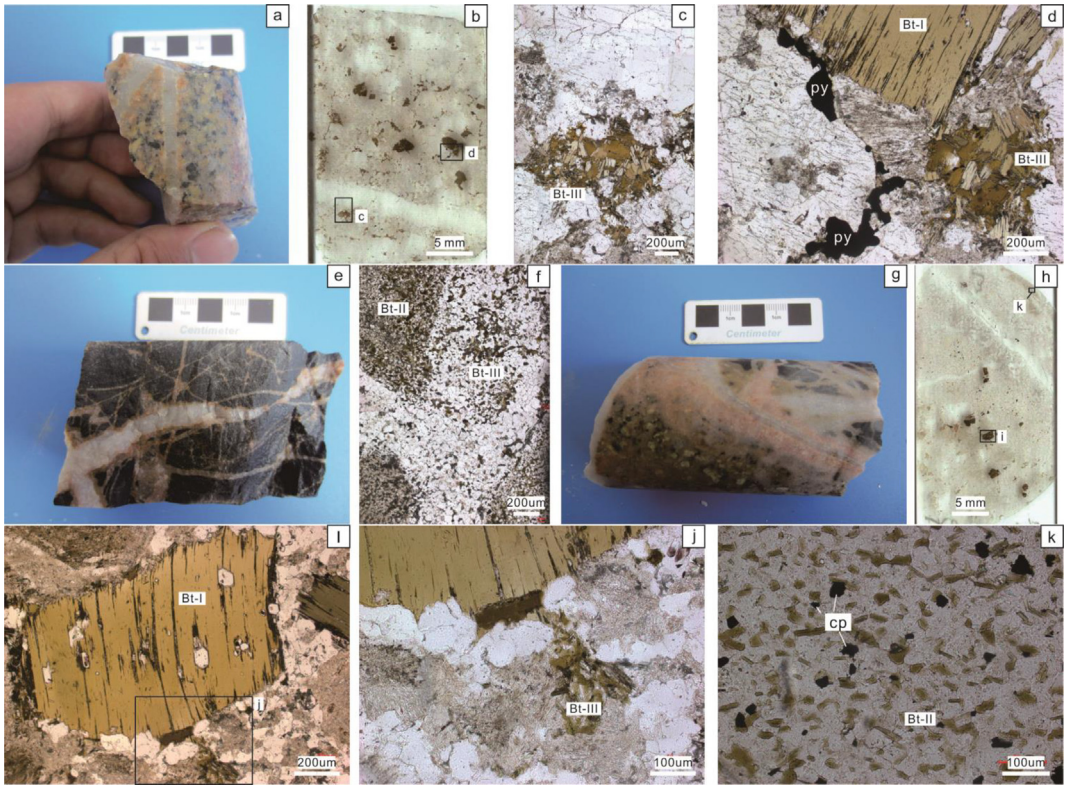

Fig. 5.1. (a, b) The Yuanzhuding granite porphyry cut by a quartz-K-feldspar vein. (c) Bt-III distributed along quartz-K-feldspar veins. (d) Bt-I phenocryst and Bt-III alteration. (e, f) Hornfels cut by a quartz-K-feldspar-biotite vein. (g, h) The contact zone between the Yuanzhuding granite porphyry and the hornfels with successive hydrothermal veins. (i, j) Bt-I phenocryst and Bt-III alteration. (k) Hornfels with disseminated chalcopyrite. a, b, c, d from ZK0-112-02. e, f from ZK0-112-03. g, h, i, j, k from ZK0-112-05b. mb = molybdenite, py = pyrite, cp = chalcopyrite.

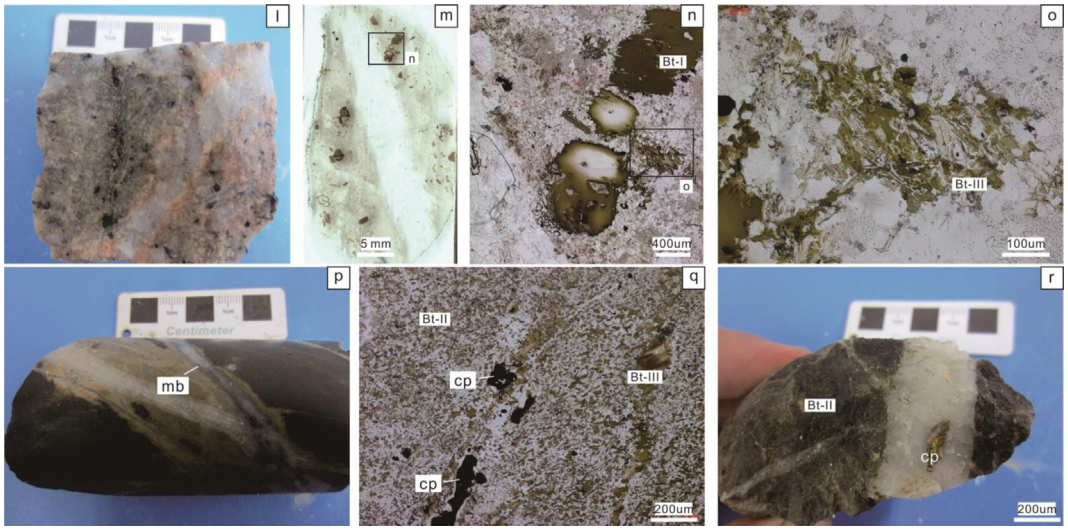

Fig. 5.2. (l, m, n) The Yuanzhuding granite porphyry cut by a quartz-K-feldspar vein. Bt-I phenocrysts are strongly altered. (o) Bt-III distributed along a quartz-K-feldspar vein. (p, q) Hornfels with disseminated Bt-II and quartz-biotite veins. (r) Bt-III in a quartz-biotite vein. l, m, n, o from ZK11-112-17. p, q from ZK11-112-21. r from ZK15-104-04. mb = molybdenite, py = pyrite, cp = chalcopyrite.

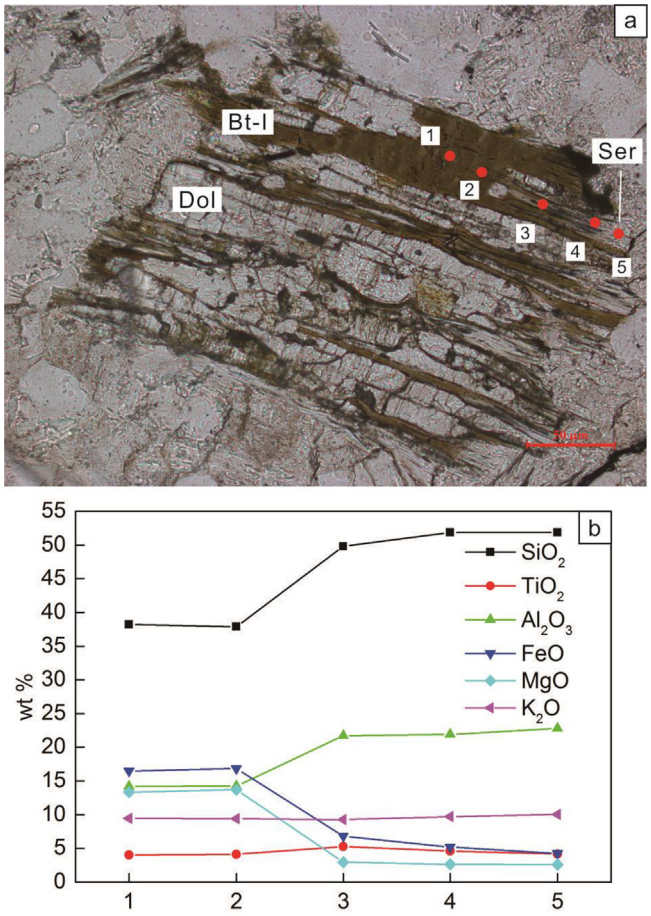

Fig. 6. (a) A Bt-I crystal partly altered to sericite and dolomite (ZK0-112-05b). (b) Variation of major element oxide contents in the altered Bt-I crystal.

3.2.3. LA-ICP-MS

LA-ICP-MS analysis of quartz trace elements were conducted with a Geolas Pro 193 nm laser system coupled with an Agilent 7900 ICP-MS at the SKLODG. Laser energy was set at 10 J/cm^2, laser repetition rate was 10 Hz, and laser spot size was set as 40 μm. Helium was used as the carrier gas and mixed with argon before entering the torch. Thirty seconds of background signal and 60 s of ablation were collected for each analysis. The following isotopes were monitored including ^{7}Li, ^{23}Na, ^{27}Al, ^{29}Si, ^{30}Si, ^{39}K, ^{43}Ca, ^{49}Ti, ^{55}Mn, ^{56}Fe, ^{63}Cu, ^{71}Ga, ^{74}Ge, ^{75}As, ^{88}Sr, ^{121}Sb, ^{137}Ba, and ^{208}Pb. The detailed method was described in Lan et al. (2017a,b). Data was reduced with ICPMSDataCal using ^{30}Si as the internal standard assuming stoichiometric quartz (Liu et al., 2008; Chen et al., 2011). NIST 610 was used as the external standard with element concentrations from Jochumet al. (2011). A natural quartz standard was used as a secondary standard to ensure accurate results for most trace elements of interest (Audétat et al., 2008). Our results on this standard consistently lie within the error range of the preferred values for Li, Ti, Al, and Ge.

3.2.4. Fluid inclusion microthermometry

A Linkam fluid inclusion cooling-heating system was used for the fluid inclusion microthermometry study at the SKLODG. The Linkam stage was calibrated at -56.6 °C, 0.0 °C, and + 374.1 °C with synthetic fluid inclusions. The precision of temperature measurements on cooling and heating runs are ± 0.1 °C and ± 2 °C, respectively. A heating rate of < 0.1 °C/s was used for ice melting temperatures. Heating rate for homogenization temperatures was no more than 1 °C/s. Heating cycles were used to determine the clathrate melting temperature in CO_2-bearing inclusions.

Fluid inclusion data were acquired on fluid inclusion assemblages (Goldstein and Reynolds, 1994) where inclusions in an assemblage display similar phase proportions and microthermometric behavior, indicating that they were trapped coevally. Homogenization temperatures of each fluid inclusion assemblage lie within a range of 10 °C, while ice melting temperatures lie within a range of 2 °C, indicating that the inclusions trapped the same fluid.

Nearly all of the vapor-liquid fluid inclusions formed clathrate upon cooling, therefore, the salinities, CO_2 contents, and densities of these inclusions were calculated with the computer program ICE (Bakker, 1997) and the data of Duan et al. (1992a,b). Isochores were calculated for all the inclusions with the computer program ISOC (Bakker, 1997) and the data of Bowers and Hegeson (1983).

3.2.5. Hydrogen and oxygen isotope

Hydrogen and oxygen isotope analysis of hydrothermal quartz and biotite (Bt-III) were carried out with a Finnigan MAT-253 isotope ratio mass spectrometer in the Analytical Laboratory of the Beijing Research Institute of Uranium Geology. To avoid the mixture of quartz and

biotite formed in the magmatic stage and metamorphic stage, quartz-bearing veins were cut from the hand samples for mineral selection. Veins were crushed and hand-picked to acquire hydrothermal quartz and biotite to the purity of over 99%. Hydrogen isotope of biotite was measured with the high temperature (1450 °C) reduction method (Sharp et al., 2001). Biotite was heated by CO_2 laser and reacted with the ClF_3 reagent to release O_2 (Sharp, 1990). The O_2 was then reacted with a hot carbon rod in the presence of platinum to get CO_2 for measurement of oxygen isotope. Fluid inclusions in quartz were decrepitated by heating to above 500 °C. The released fluid was then reacted with chromium powder to obtain H_2 for isotopic analysis (Wan et al., 2005). Oxygen of quartz was liberated by the reaction with BrF_2 and then converted to CO_2 on a platinum coated carbon rod for oxygen isotope analysis (Clayton and Mayeda, 1963). The hydrogen and oxygen isotope results were reported relative to the V-SMOW, and the analytical precisions were ± 0.2‰ for $\delta^{18}O$ and ± 2‰ for δD values.

4. Results

4.1. Mica petrography

Micas in the Yuanzhuding porphyry Cu-Mo deposit can be divided into four types including magmatic biotite (Bt-I), metamorphic biotite (Bt-II), hydrothermal biotite (Bt-III), and hydrothermal sericite (Ser), based on the detailed petrographic study (Figs. 4, 5, 6).

Bt-I refers to the magmatic biotite directly crystalized from the silicate melt and occurs as phenocrysts in the Yuanzhuding granite porphyry. Bt-I displays euhedral crystal shapes with grain sizes ranging from < 1 mm to ~3 mm, and locally displaying irregular boundaries where strong alteration took place (Figs. 5.1a, b, d, i, 5.2m, n). A small amount of magmatic biotite is also randomly distributed in the matrix with a grain size < 0.1 mm.

Bt-II stands for metamorphic biotite formed during the contact metamorphism caused by the intrusion of the Yuanzhuding granite porphyry into the Upper Cambrian Shuikou Group. Bt-II is occurring only in the hornfels close to the granite porphyry with grain size < 100 μm (Figs. 5e, f, g, k, 5.2p, q).

Bt-III represents hydrothermal biotite crystalized in the potassic alteration stage. This biotite type is mainly distributed within the Yuanzhuding granite porphyry as randomly oriented aggregates of finer-grained flakes along the quartz-K-feldspar veins (Figs. 5c, d, f, 5.2n, o). It can also be found in the hornfels as quartz-biotite veins (Fig. 5.2p, q, r). Grain sizes of Bt-III are around several tens to several hundreds of micrometers.

Ser refers to hydrothermal sericite formed in the sericitic alteration stage of the hydrothermal fluid evolution (Fig. 4.2j, k). Sericite is in parts an alteration product of pre-existing biotite (Fig. 6). The abundance of Ser generally increases with increasing distance from the center of the granite porphyry (Figs. 3, 5).

4.2. Mica compositions

Although the electron microprobe analysis (EMPA) method is not capable of determining light elements, such as H, or distinguishing ferrous iron and ferric iron, the normalization procedures can turn the analytical results into the crystallochemical formula that can be used to evaluate the hydrogen content and the oxidation state of iron (Czamanske and Wones, 1973; Parry et al., 1978). The continuous revisions to the normalization procedures in the past few decades have led to a better identification of mica structures (Dymek, 1983; Tindle and Webb, 1990; Feldstein et al., 1996; Tischendorf et al., 1997, 1999, 2001; Rieder et al., 1998; Rieder, 2001).

Table 1 presents average EMPA data and the calculated parameters of each mica type in 12 samples. Calculated average X_{Mg} numbers in Bt-I, Bt-II, and Bt-III are ~0.53 ± 0.03, ~0.51 ± 0.03, and ~0.56 ± 0.06, respectively (Fig. 7). Average X_{Mg} of Ser is ~0.07 ± 0.02 (Fig. 8). The average SiO_2 content is ~37.81 ± 1.28 wt% in Bt-I, Bt-II, and Bt-III, and increases to ~49.05 ± 2.63 wt% in Ser. Average TiO_2 contents decrease from ~4.09 ± 0.22 wt% in Bt-I to ~3.05 ± 0.59 wt% in Bt-II to ~2.97 ± 0.67 wt% in Bt-III, and to 0.50 ± 0.16 wt% in Ser (Figs. 7a, 8a). Average Al_2O_3 contents increase from ~13.81 ± 0.23 wt% in Bt-I to ~16.51 ± 1.33 wt% in Bt-II, then decrease to ~14.31 ± 0.83 wt% in Bt-III (Fig. 7b). Ser contains average Al_2O_3 of ~30.26 ± 3.03 wt% (Fig. 8b). FeO contents decrease slightly from ~14.96 ± 1.50 wt% in Bt-I to ~14.80 ± 1.67 wt% in Bt-II to ~13.76 ± 2.44 wt% in Bt-III. In sericite it is ~2.39 ± 0.46 wt% (Fig. 8c). Average MgO contents decrease from ~14.73 ± 0.94 wt% in Bt-I to ~13.59 ± 1.05 wt% in Bt-II, then increases to ~15.49 ± 2.07 wt% in Bt-III (Fig. 7d). Average MgO content in Ser is ~1.84 ± 0.69 wt% (Fig. 8d). Average K_2O contents are identical in Bt-I, Bt-II, Bt-III, and Ser at ~10.07 ± 0.41 wt% (Figs. 7e, 8e). Average F contents decrease from ~0.52 ± 0.10 wt% in Bt-I to ~0.43 ± 0.09 wt% in Bt-II, then increase to ~0.58 ± 0.21 wt% in Bt-III (Fig. 7f). Average F content in Ser is ~0.19 ± 0.11 wt% (Fig. 8f). Average Cl contents are ~0.01 ± 0.01 wt% in Bt-I, ~0.05 ± 0.01 wt% in Bt-II, ~0.04 ± 0.02 wt% in Bt-III, and ~0.01 ± 0.00 wt% in Ser (Table 1).

Although it is not clear in each biotite type, there is generally a positive correlation between the X_{Mg} number and the F content in all biotite spots. The average total of all mica types is ~96 wt%, with the remaining 4 wt% possibly being H_2O, Li_2O, and other components that cannot be measured by EMPA.

All the biotite data plot in the Mg-biotite zone in the (Mg-Li) vs (Fe_{tot} + Mn + Ti - Al^{VI}) diagram, and all the Ser is located in the transition zone from Li-muscovite to Li-phengite (Fig. 9a). Fig. 9b illustrates a detailed distribution of biotite composition in the Mg-biotite zone, in which each type of biotite displays a general negative correlation in the (Mg-Li) vs (Fe_{tot} + Mn + Ti - Al^{VI}) diagram. Bt-I lies close to the upper-right corner; Bt-II lies close the lower-left corner; and Bt-III lies in the middle.

4.3. Quartz CL textures and compositions

SEM-CL analysis revealed that quartz-bearing veins with potassic alteration consistently show granular mosaic texture with generally homogeneous brightness (Fig. 10a, b, c). In contrast, quartz in veins with sericitic alteration is typically euhedral with growth zones of oscillating CL intensity and some crystals also display sector zoning (Fig. 10d, e).

Two representative samples (ZK0-112-03, ZK15-104-04) were analyzed by LA-ICP-MS for trace element concentrations (Table 2; See Section 3.1 for sample description). Mineral and fluid inclusions are ways for elements to be incorporated in hydrothermal quartz analysis and are regarded as contamination for our analysis. The raw data acquired by LA-ICP-MS were carefully reduced to avoid the contamination from fluid and mineral inclusions.

Numerous previous studies have shown that Ti, Li, Al, and Ge are structurally hosted in quartz, and they can reflect the physical and chemical conditions of quartz formation (Larsen et al., 2000; Müller et al., 2003, 2012; Götze et al., 2004; Landtwing and Pettke, 2005; Rusk, 2006; Jacamon and Larsen, 2009; Lehmann et al., 2009; Donovan et al., 2011; Götte et al., 2011; Breiter et al., 2013; Audétat et al., 2008; Maydagán et al., 2015; Mao et al., 2017). Although Na, K, Ca, Mn, Fe, Pb, etc., are possible to be presented in quartz, they are much more abundant in fluid and mineral inclusions. Table 2 clearly shows that, except for Ti, Li, Al, and Ge, nearly all the other elements are below or close to the detection limits, indicating that the interferences from mineral and fluid inclusions are negligible and the data are representatives of the trace element contents in quartz.

Sample ZK0-112-03: Ti contents range from 25.0 to 36.3 ppm with an average of ~31.1 ppm. Li contents vary from 2.85 to 8.14 ppm with an average of 5.52 ppm. Al contents range from 48 to 101 ppm with an average of ~66 ppm. Ge contents range from 0.55 to 1.29 ppm with an

Table 1
Average EMPA data and the calculated parameters of each mica type from 12 samples in the Yuanzhuding porphyry Cu-Mo deposit.

Sample NO.	1	3	6	20	2	3	4	9	12
Sample name	ZK0-112-02	ZK0-112-05	ZK11-112-17	ZK0-112-01	ZK0-112-03	ZK0-112-05	ZK0-112-08	ZK11-112-21	ZK26-100-05
NO. of spots	11	9	8	9	6	3	2	6	6
Mica type	Bt-I	Bt-I	Bt-I	Bt-I	Bt-II	Bt-II	Bt-II	Bt-II	Bt-II
SiO_2	38.65	37.94	38.08	37.87	34.91	37.22	38.53	36.90	36.74
TiO_2	4.17	4.15	3.74	4.32	2.95	4.00	3.14	3.02	2.15
Al_2O_3	13.96	13.70	13.49	14.09	17.24	14.88	15.52	16.24	18.65
FeO	13.01	16.45	16.38	13.98	17.79	14.39	12.70	14.99	14.12
MnO	0.08	0.17	0.13	0.09	0.11	0.17	0.11	0.12	0.07
MgO	15.88	13.62	14.00	15.41	11.63	13.82	14.76	13.70	14.03
CaO	0.02	0.02	0.03	0.02	LOD	LOD	0.09	LOD	LOD
Na_2O	0.14	0.17	0.12	0.17	0.11	0.09	0.12	0.12	0.13
K_2O	9.92	9.58	9.51	9.64	10.30	10.18	9.96	9.93	10.05
BaO	0.32	0.36	0.30	0.36	0.25	0.33	0.30	0.25	0.16
F	0.64	0.36	0.55	0.54	0.34	0.31	0.54	0.48	0.47
Cl	0.05	0.05	0.08	0.04	0.06	0.07	0.04	0.05	0.04
Total	96.82	96.57	96.41	96.54	95.70	95.46	95.81	95.79	96.61
Si	2.84	2.84	2.86	2.81	2.67	2.80	2.85	2.77	2.71
Al(IV)	1.16	1.16	1.14	1.19	1.33	1.20	1.15	1.23	1.29
Al(VI)	0.05	0.05	0.05	0.04	0.22	0.12	0.21	0.20	0.33
Ti	0.23	0.23	0.21	0.24	0.17	0.23	0.18	0.17	0.12
Fe^{3+}	0.19	0.22	0.22	0.29	0.10	0.11	0.08	0.07	0.05
Fe^{2+}	0.61	0.81	0.81	0.58	1.03	0.80	0.71	0.87	0.82
Fe^{3+}(M)	0.19	0.22	0.22	0.29	0.10	0.11	0.08	0.07	0.05
Mn	0.01	0.01	0.01	0.01	0.01	0.01	0.01	0.01	0.00
Mg	1.74	1.52	1.57	1.70	1.33	1.55	1.63	1.53	1.54
Ca	0.00	0.00	0.00	0.00	–	–	0.01	–	–
Na	0.02	0.02	0.02	0.02	0.02	0.01	0.02	0.02	0.02
K	0.93	0.91	0.91	0.91	1.01	0.98	0.94	0.95	0.95
Ba	0.01	0.01	0.01	0.01	0.01	0.01	0.01	0.01	0.00
OH	1.84	1.91	1.86	1.87	1.91	1.92	1.87	1.88	1.89
F	0.15	0.09	0.13	0.13	0.08	0.07	0.13	0.11	0.11
Cl	0.01	0.01	0.01	0.01	0.01	0.01	0.01	0.01	0.01
mgli	1.51	1.32	1.36	1.51	1.25	1.38	1.40	1.38	1.40
feal	0.98	1.23	1.20	1.08	1.09	1.02	0.76	0.92	0.66
Li_2O	1.54	1.34	1.38	1.32	0.47	1.13	1.51	1.04	0.99
X_{Mg}	0.57	0.50	0.51	0.56	0.45	0.52	0.54	0.51	0.51
X_{Sid}	0.16	0.19	0.17	0.18	0.40	0.24	0.24	0.30	0.37
X_{Ann}	0.27	0.31	0.32	0.26	0.15	0.24	0.23	0.19	0.12
X_{OH}	0.92	0.95	0.93	0.93	0.96	0.96	0.93	0.94	0.94
X_F	0.07	0.04	0.06	0.06	0.04	0.04	0.06	0.06	0.05
X_{Cl}	0.00	0.00	0.01	0.00	0.00	0.00	0.00	0.00	0.00
IV(F)	2.13	2.45	2.13	2.18	2.30	2.88	2.13	2.21	2.14
IV(Cl)	−3.55	−3.51	−3.71	−3.49	−3.44	−3.66	−3.44	−3.49	−3.36
IV(F/Cl)	5.67	5.96	5.84	5.67	5.75	6.55	5.57	5.70	5.50
$logX_F/X_{OH}$	−1.12	−1.52	−1.19	−1.18	−1.47	−1.94	−1.17	−1.29	−1.24
$logX_{Cl}/X_{OH}$	−2.56	−2.46	−2.29	−2.59	−2.44	−2.35	−2.61	−2.50	−2.64
$logX_F/X_{Cl}$	1.44	0.94	1.10	1.41	0.96	0.41	1.44	1.21	1.39
Temperature (°C)									
$logf(H_2O)f(HF)^{fluid}$									
$logf(H_2O)/f(HCl)^{fluid}$									
$logf(HF)/f(HCl)^{fluid}$									

Sample NO.	1	2	3	6	9	10	2	3	5	11	12
Sample name	ZK0-112-02	ZK0-112-03	ZK0-112-05	ZK11-112-17	ZK11-112-21	ZK15-104-04	ZK0-112-03	ZK0-112-05	ZK11-112-02	ZK22-106-09	ZK26-100-05
NO. of spots	9	2	4	3	2	5	4	3	4	3	7
Mica type	Bt-III	Bt-III	Bt-III	Bt-III	Bt-III	Bt-III	Ser	Ser	Ser	Ser	Ser
SiO_2	39.26	36.20	39.04	39.29	37.15	39.73	51.98	52.13	48.74	46.05	46.35
TiO_2	3.28	4.17	3.06	2.78	2.55	2.00	0.51	0.36	0.32	0.76	0.54
Al_2O_3	13.70	14.73	13.85	13.24	15.79	14.55	26.89	29.00	27.68	33.73	34.02
FeO	12.15	16.99	14.88	15.73	13.21	9.61	1.86	2.09	3.22	2.44	2.35
MnO	0.08	0.09	0.09	0.15	0.10	0.08	0.01	0.01	LOD	0.01	0.01
MgO	16.80	12.57	14.97	14.48	14.89	19.22	2.71	2.21	2.23	0.99	1.06
CaO	0.05	0.01	0.05	0.01	0.01	0.02	0.06	0.06	0.03	0.01	LOD
Na_2O	0.14	0.09	0.14	0.13	0.10	0.11	0.04	0.09	0.10	0.44	0.40
K_2O	9.86	10.28	9.82	9.74	9.84	9.91	10.72	10.11	11.13	10.15	10.83
BaO	0.28	0.35	0.26	0.22	0.21	0.17	0.05	0.01	0.02	0.06	0.05

(*continued on next page*)

Table 1 (*continued*)

Sample NO.	1	2	3	6	9	10	2	3	5	11	12
F	0.72	0.31	0.52	0.55	0.44	0.95	0.26	0.23	0.32	0.08	0.04
Cl	0.04	0.04	0.03	0.07	0.02	0.02	0.01	0.02	0.01	0.01	0.01
Total	96.36	95.83	96.71	96.37	94.30	96.37	95.10	96.33	93.81	94.73	95.66
Si	2.89	2.75	2.89	2.93	2.80	2.89	3.47	3.42	3.35	3.10	3.10
Al(IV)	1.11	1.25	1.11	1.07	1.20	1.12	0.53	0.58	0.65	0.90	0.90
Al(VI)	0.07	0.08	0.10	0.09	0.21	0.13	1.58	1.66	1.59	1.78	1.78
Ti	0.18	0.24	0.17	0.16	0.15	0.11	0.03	0.02	0.02	0.04	0.03
Fe^{3+}	0.10	0.20	0.06	0.04	0.03	0.06	0.00	0.00	0.00	0.00	0.00
Fe^{2+}	0.65	0.88	0.86	0.94	0.80	0.52	0.10	0.12	0.19	0.14	0.13
Fe^{3+}(M)	0.10	0.20	0.06	0.04	0.03	0.06	0.00	0.00	0.00	0.00	0.00
Mn	0.01	0.01	0.01	0.01	0.01	0.01	0.00	0.00	–	0.00	0.00
Mg	1.84	1.43	1.65	1.61	1.67	2.08	0.27	0.22	0.23	0.10	0.11
Ca	0.00	0.00	0.00	0.00	0.00	0.00	0.00	0.00	0.00	0.00	0.00
Na	0.02	0.01	0.02	0.02	0.01	0.02	0.01	0.01	0.01	0.06	0.05
K	0.93	1.00	0.93	0.93	0.95	0.92	0.91	0.85	0.97	0.87	0.92
Ba	0.01	0.01	0.01	0.01	0.01	0.00	0.00	0.00	0.00	0.00	0.00
OH	1.83	1.92	1.87	1.86	1.89	1.78	1.94	1.95	1.93	1.98	1.42
F	0.17	0.07	0.12	0.13	0.11	0.22	0.06	0.05	0.07	0.02	0.01
Cl	0.01	0.01	0.00	0.01	0.00	0.00	0.00	0.00	0.00	0.00	0.00
mgli	1.59	1.30	1.41	1.35	1.51	1.81	−0.45	−0.50	−0.38	−0.40	−0.40
feal	0.86	1.25	1.00	1.05	0.78	0.57	−1.45	−1.53	−1.39	−1.60	−1.62
Li_2O	1.72	0.84	1.65	1.72	1.11	1.85	5.37	5.41	4.44	3.66	3.75
X_{Mg}	0.59	0.48	0.53	0.52	0.55	0.65	0.10	0.08	0.09	0.04	0.04
X_{Sid}	0.13	0.27	0.16	0.13	0.26	0.14	0.70	0.77	0.79	0.96	0.96
X_{Ann}	0.28	0.25	0.30	0.35	0.19	0.21	0.20	0.15	0.13	0.00	0.00
X_{OH}	0.91	0.96	0.94	0.93	0.95	0.89	0.97	0.98	0.96	0.99	0.99
X_F	0.08	0.04	0.06	0.06	0.05	0.11	0.03	0.02	0.04	0.01	0.01
X_{Cl}	0.00	0.00	0.00	0.00	0.00	0.00	0.00	0.00	0.00	0.00	0.00
IV(F)	2.09	2.34	2.19	2.12	2.25	2.04	2.11	2.03	1.80	2.69	3.02
IV(Cl)	−3.39	−3.40	−3.28	−3.66	−3.13	−3.29	−2.04	−2.11	−2.03	−1.66	−1.89
IV(F/Cl)	5.49	5.73	5.47	5.78	5.38	5.33	4.15	4.14	3.82	4.35	4.91
$logX_F/X_{OH}$	−1.05	−1.44	−1.22	−1.16	−1.28	−0.93	−1.73	−1.69	−1.45	−2.43	−2.76
$logX_{Cl}/X_{OH}$	−2.76	−2.55	−2.76	−2.35	−2.94	−2.98	−3.16	−3.05	−3.15	−3.42	−3.20
$logX_F/X_{Cl}$	1.71	1.10	1.54	1.19	1.67	2.06	1.43	1.36	1.70	0.99	0.43
Temperature (°C)	575	575	575	575	575	575					
$logf(H_2O)f(HF)^{fluid}$	5.04	5.29	5.13	5.06	5.22	5.00					
$logf(H_2O)/f(HCl)^{fluid}$	5.18	4.89	5.14	4.72	5.34	5.44					
$logf(HF)/f(HCl)^{fluid}$	−0.63	−1.02	−0.69	−1.01	−0.59	−0.40					

Notes: 1. Mgli = [Mg-Li]; feal = [Fe_{tot} + Mn + Ti − Al^{VI}]. 2. Empirical equation [$Li_2O = (0.287*SiO_2) - 9.552$] proposed by Tindle and Webb (1990) is used as a calculation scheme under major oxides caption. 3. X_{Mg} = Mg/(sum octahedral cations); $X_{Sid} = [(3 - Si/Al)/1.75](1 - X_{Mg})$; $X_{An} = 1 - X_{Mg} - X_{Sid}$. 4. LOD = below detection limits.

average of ~1.04 ppm (Fig. 11).

Sample ZK15-104-04: Ti contents vary widely from 2.9 to 26 ppm with an average of ~11.6 ppm. Li contents vary from 1.04 to 17.1 ppm with an average of 5.04 ppm. Al contents vary from 14 to 243 ppm with an average of ~66 ppm. Ge concentrations range from 1.58 to 3.85 ppm with an average of ~2.12 ppm (Fig. 11).

4.4. Fluid inclusion petrography and microthermometry

Fluid inclusions in many quartz-bearing veins have experienced post-entrapment modification. Therefore, we have only conducted fluid inclusion microthermometry on two samples where inclusions are well preserved (ZK0-112-03, ZK15-104-04; Figs. 12, 13; Table 3; See Section 3.1 for sample description).

Sample ZK0-112-03: The majority of the primary fluid inclusions are vapor-liquid inclusions at room temperature. The volume ratios of the vapor phase range generally from 40 to 55 vol%, with the majority of them lying between 45 and 50 vol% (Table 3). CO_2-rich fluid inclusions, where liquid and gaseous CO_2 are both presented at room temperature, have been randomly observed. Ice-melting temperatures of the vapor-liquid fluid inclusions range from -2.5 to -5.8 °C, with an average of ~-4.4 °C. Nearly all the fluid inclusions formed clathrate upon cooling, indicating that the hydrothermal fluid contains CO_2. Clathrate melting temperatures range from 7.9 to 9.6 °C, with an average of ~8.7 °C. Homogenization temperatures range from 284 to 343 °C, with the peak at ~310 to 330 °C. The calculated salinities based upon clathrate melting temperatures range from 0.8 to 4.1 wt% NaCl equiv., with an average of ~2.5 wt%. The hydrothermal fluid contains 2.2 to 3.2 mol % CO_2, with an average of ~2.6 mol %. Calculated fluid densities range from 0.50 to 0.65 g/cm^3, with an average of ~0.60 g/cm^3.

Sample ZK15-104-04: All the primary fluid inclusions are vapor-liquid inclusions at room temperature. The volume ratios of the vapor phase generally vary from 15 to 30 vol%, with an average of ~25 vol%. Ice-melting temperatures of the vapor-liquid fluid inclusions vary from -3.1 to -5.3 °C, with an average of ~-4.5 °C. The majority of these fluid inclusions formed clathrate upon cooling, indicating that the hydrothermal fluid contains some extent of CO_2. Clathrate melting temperatures vary from 7.6 to 9.2 °C, with an average of ~8.6 °C. Homogenization temperatures vary from 248 to 295 °C, with the peak at ~270 to 290 °C. The calculated salinities based upon clathrate melting temperatures vary from 1.6 to 4.7 wt% NaCl equiv., with an average ~2.8 wt%. The hydrothermal fluid contains 1.7 to 2.0 mol % CO_2, with an average of ~1.8 mol %. Calculated fluid densities vary from 0.74 to 0.83 g/cm^3, with an average of ~0.78 g/cm^3.

4.5. Hydrogen and oxygen isotopes

Table 4 reports the δD and $\delta^{18}O$ values of mica and quartz. The δD values of hydrothermal biotite (Bt-III) vary from -85.2‰ to -93.0‰, with an average of ~-87.7‰. The $\delta^{18}O$ values of biotite are 6.5‰ to 7.0‰, with an average of ~6.7‰. The δD values from fluid inclusions

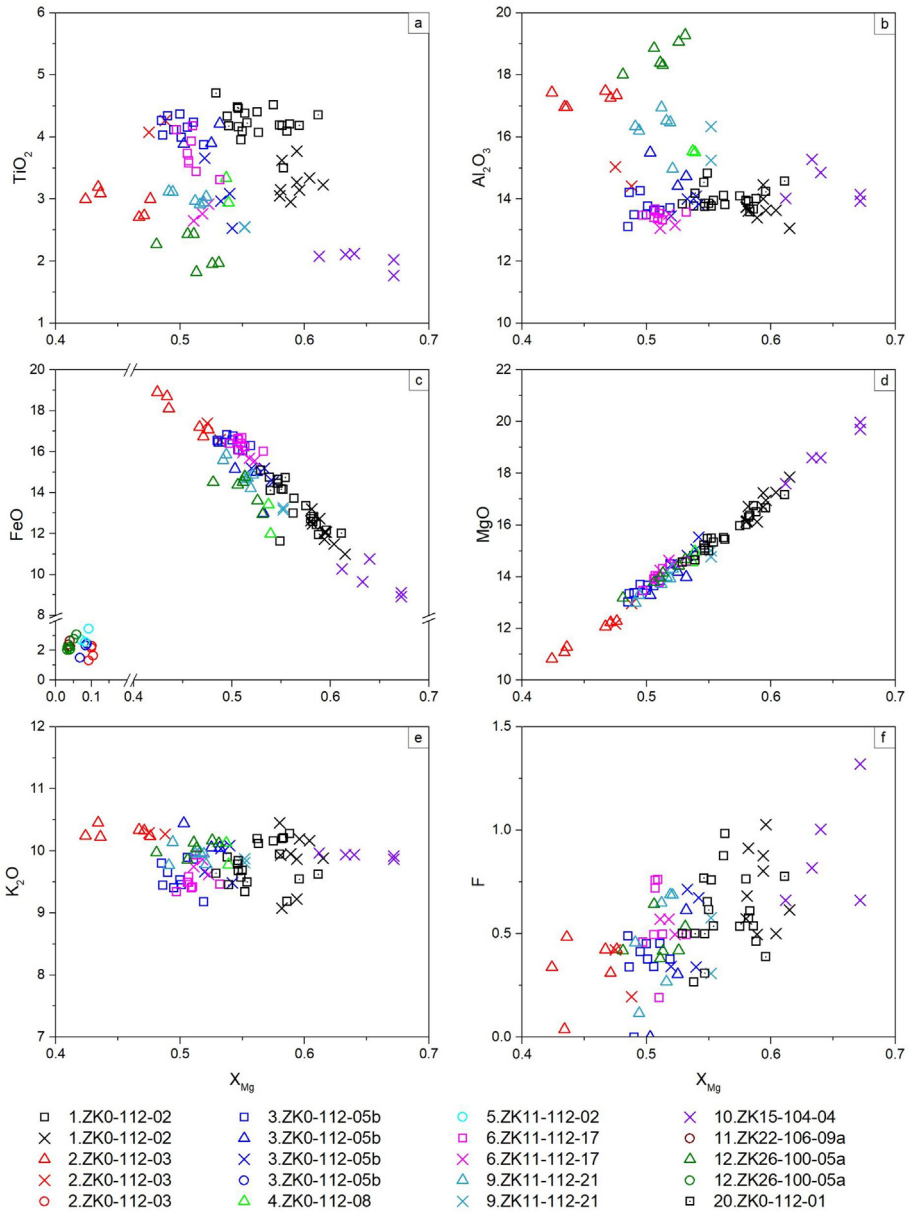

Fig. 7. Variation of TiO_2, Al_2O_3, FeO, MgO, K_2O, and F contents with X_{Mg} of mica in the Yuanzhuding porphyry deposit. Squares refer to Bt-I; Triangles refer to Bt-II; Crosses refer to Bt-III. Circles refer to sericite. Different samples are distinguished by color.

in quartz are on average ~-54.3‰ in drill hole ZK0-112, ~-64.1‰ in drill hole ZK11-112, and -64.0‰ in drill hole ZK15-104, -64.2‰ in drill hole ZK22-106, and -70.3‰ in drill hole ZK26-100. The δD values of water generally decrease with the increasing distance from the porphyry center. The $\delta^{18}O$ values of quartz are on average ~9.4‰ in drill hole ZK0-112, ~10.4‰ in drill hole ZK11-112, 11.9‰ in drill hole ZK15-104, 13.4‰ in drill hole ZK22-106, and 10.5‰ in drill hole ZK26-100. The $\delta^{18}O$ values of quartz generally increase with increasing distance from the porphyry center.

5. Discussion

5.1. Influence of hydrothermal alteration to mica compositions

Biotite compositions are apt to be altered by the successive hydrothermal fluid events, therefore, fresh biotite crystals with euhedral crystal shapes and clear cleavages were cautiously selected during the EMPA analysis to avoid the compositional change caused by alteration. To evaluate the influence of hydrothermal alteration by sericitic alteration, we studied some biotite crystals partly altered to sericite. Fig. 6 displays a Bt-I crystal partly altered to sericite and dolomite. An EMPA profile analysis clearly demonstrates the notable increase of SiO_2 and Al_2O_3, and decrease of FeO and MgO during the alteration from biotite to sericite. The K_2O and TiO_2 contents remain nearly constant after the hydrothermal alteration. However, compared with the rather low TiO_2 contents in all the other Ser spots (Fig. 6b), we interpret the elevated TiO_2 concentration to be related to the incomplete alteration.

All the Ser spots plot in the lower left corner in Fig. 7c, and because Mg can substitute Fe in the M site, the biotite spots plot in the upper right corner with a negative correlation between X_{Mg} and FeO*. The scattered biotite data pointing to the lower left corner are likely related to the sericitic alteration, although the majority of the biotite data are confident to represent the primary compositions.

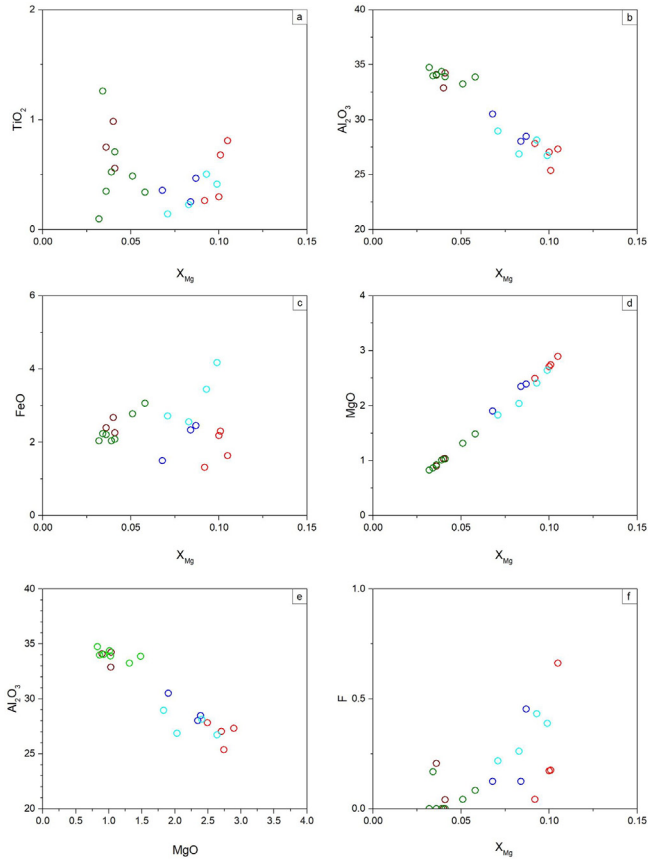

Fig. 8. Variation of TiO_2, Al_2O_3, FeO, MgO, and F contents with X_{Mg} of sericite in the Yuanzhuding porphyry deposit. Different samples are distinguished by color. See detailed legends in Fig. 7.

5.2. Element content variations of micas and quartz

Variations of TiO_2, Al_2O_3, K_2O, etc. in Bt-I are small compared to Bt-II and Bt-III, likely because they were crystalized from the relatively homogeneous magmatic conditions (Fig. 7). As Ti content in biotite is proportional to temperature (Wones and Eugster, 1965; Beane, 1974; Henry, 2005; Nachit et al., 2005; Parsapoor et al., 2015), the higher contents of TiO_2 in Bt-I relative to Bt-II and Bt-III generally reflect the higher temperature of crystallization. The larger variations of TiO_2 contents in Bt-II and Bt-III are likely related to wider temperature range of biotite formation (See discussion below). Average Al_2O_3 content of Bt-III is similar to that of Bt-I but shows slightly larger variation. In contrast, Al_2O_3 content in Bt-II is much higher than Bt-I and Bt-III, and it also exhibits much larger variation. As the Bt-II was formed by contact metamorphism of the preexisting sedimentary rocks, we infer that the higher content of Al_2O_3 may indicate that Al was more readily available during the contact metamorphism to form Bt-II, and the larger variation of Al_2O_3 may be related to the inhomogeneous property of the Upper Cambrian Shuikou group.

The TiO_2, FeO, and F contents in sericite show no relationship with the variation of X_{Mg} (Fig. 8a, c, f). In contrast, linear correlations are revealed among X_{Mg}, Al_2O_3, and MgO contents. The X_{Mg} values and MgO concentrations in sericite generally decrease with the increasing distances from the Yuanzhuding granite porphyry (Fig. 8d). In contrast, the Al_2O_3 contents increase with the increasing distances from the ore-forming intrusion. As Mg and Al can be incorporated in the M site in mica, the negative correlation between Al_2O_3 and MgO clearly show that the above element content variations are caused by the substitution of Mg by Al in the M site of sericite.

Trace element concentrations in quartz from ZK0-112-03 are generally homogeneous and the variations of Ti, Li, Al, and Ge are relatively small, indicating that these elements were incorporated in quartz in equilibrium conditions (Rusk, 2012; Mao et al., 2017). In contrast, trace element concentrations in quartz from ZK15-104-04 show much larger variations. The concentrations of Li, Al, and Ge generally increase with the increase of Ti contents (Fig. 11). Positive correlations between high quartz growth rate and trace element concentrations are observed in many studies (Martin and Armington, 1983; Armington and Larkin, 1985; Armington, 1991; Watson and Liang, 1995; Watson, 1996; Watson, 2004; Jourdan et al., 2009; Huang and Audétat, 2012; Mao et al., 2017), indicating that more structural imperfections will form with faster growth rate, and therefore lead to kinetic incorporation of trace elements instead of equilibrium incorporation. We infer that the large variations of trace element contents in ZK15-104-04 indicate that they were incorporated in quartz kinetically.

5.3. Temperature of the contact metamorphism

Titanium concentrations and the Mg/Fe ratios in biotite are important factors to evaluate temperatures of crystallization (Wones and Eugster, 1965; Beane, 1974; Henry, 2005; Nachit et al., 2005; Parsapoor et al., 2015). Henry (2005) revealed that the Ti-tschermaks substitution is controlled by octahedral-tetrahedral layer misfit and is dominant in magnesian biotite, whereas Ti-deprotonation substitution prevails at intermediate X_{Mg}. An empirical Ti-in-biotite geothermometer was given by Henry (2005) for biotite in metapelites as follows:

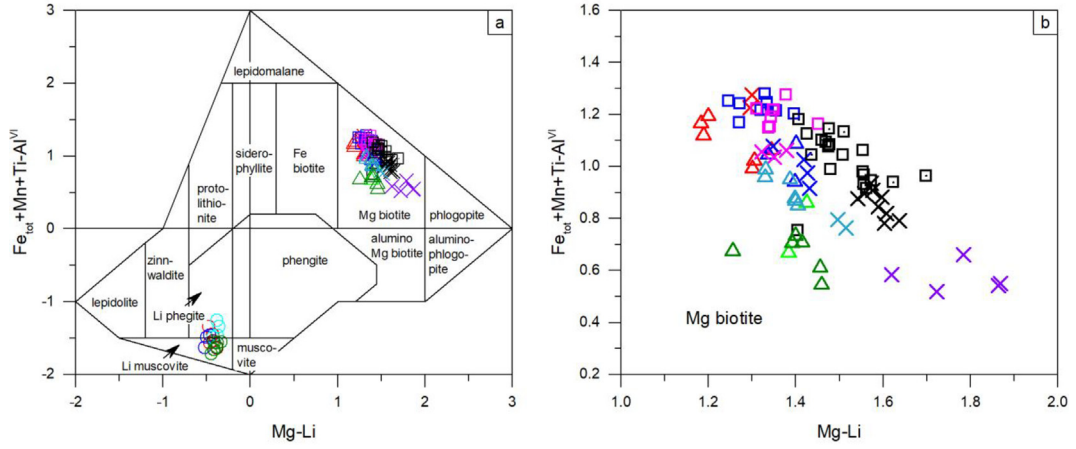

Fig. 9. (a) Plot of the Yuanzhuding micas in the (Mg-Li) vs (Fe_{tot} + Mn + Ti - Al^{VI}) classification diagram (Tischendorf et al., 1997). (b) Details of biotite from the Yuanzhuding porphyry deposit in the (Mg-Li) vs (Fe_{tot} + Mn + Ti - Al^{VI}) classification diagram. See detailed legends in Fig. 7.

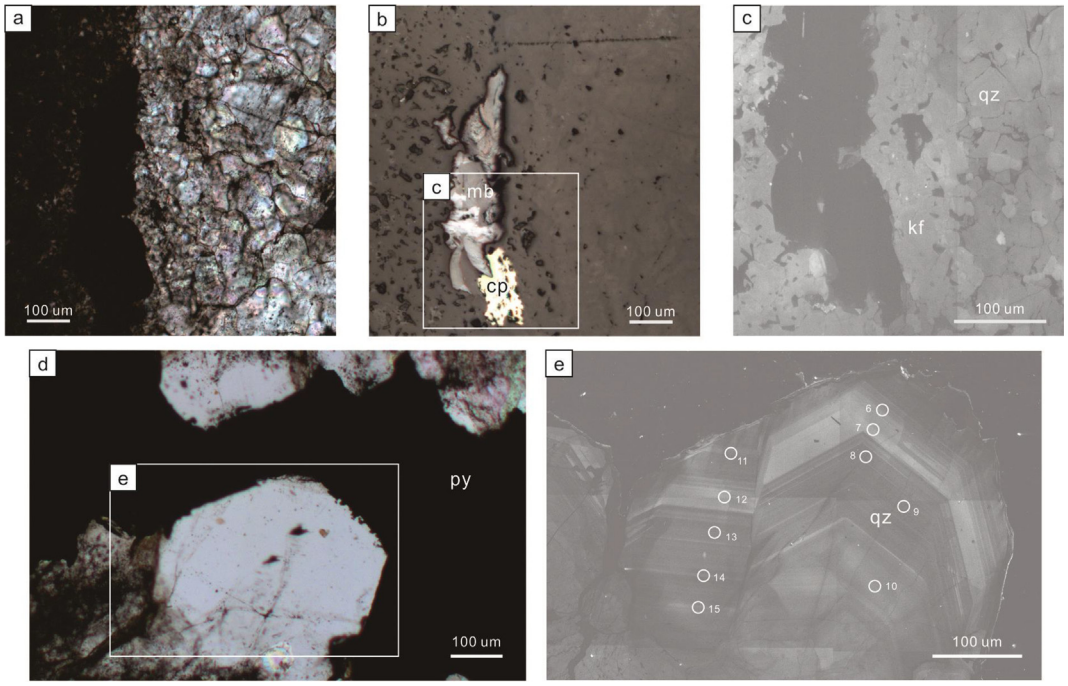

Fig. 10. Transmitted, reflected, and CL images of quartz-bearing veins in the Yuanzhuding porphyry deposit. a, b, c form sample K0-112-03. d, e from sample ZK15-104-04.

$$T = ([ln(Ti) - a - c(X_{Mg})^3]/b)^{0.333} \quad (1)$$

where a = – 2.3594, b = 4.6482 × 10^{-9}, c = – 1.7283

The compositions of Bt-II in the Yuanzhuding porphyry deposit lie within the calibrated range (X_{Mg} = 0.275 ~ 1.000, Ti = 0.04 ~ 0.60 apfu., and T = 480 ~ 800 °C). We applied the Ti-in-biotite geothermometer for the temperature calculation of Bt-II formed during the contact metamorphism (Table 5).

Crystallization temperatures of Bt-II decrease from up to ~620 °C in drill hole ZK0-112 to ~560 °C in drill hole ZK11-112 and to ~460 °C in drill hole ZK26-100 which is furthest from the porphyry center. The maximum temperature of ~620 °C in Bt-II is related to the hornfels several millimeters from the contact to the porphyry intrusion (Fig. 5.1g, h, k). Bt-II is the product of contact metamorphism, and the decreasing temperature with increasing distance from the porphyry center clearly records the outward cooling of the system during contact metamorphism (Fig. 3).

Table 2
Trace element concentrations of quartz-bearing veins in the Yuanzhuding porphyry Cu-Mo deposit.

Spots	^{49}Ti	^{7}Li	^{23}Na	^{27}Al	^{39}K	^{43}Ca	^{55}Mn	^{56}Fe	^{63}Cu	^{71}Ga	^{74}Ge	^{75}As	^{88}Sr	^{121}Sb	^{137}Ba	^{208}Pb
ZK0-112-03-1	29.4	6.07	< 0.81	56.7	< 1.95	< 71.39	< 0.59	< 2.63	< 0.09	0.02	1.29	< 0.34	0.01	< 0.03	0.01	< 0.01
ZK0-112-03-2	32.5	6.26	< 1.02	56.1	< 2.60	69.2	< 0.54	< 3.94	< 0.09	0.01	1.10	< 0.30	0.01	< 0.07	0.01	0.01
ZK0-112-03-3	34.6	3.11	4.65	101	3.48	177	< 0.48	< 2.81	< 0.13	< 0.04	1.18	< 0.24	0.98	< 0.04	0.39	0.02
ZK0-112-03-4	34.1	7.32	< 0.61	63.3	< 1.34	< 61.52	< 0.29	3.31	0.23	< 0.01	0.55	0.19	< 0.01	< 0.02	< 0.05	< 0.01
ZK0-112-03-5	32.3	7.37	1.03	66.9	< 2.31	< 69.32	< 0.47	5.05	< 0.08	0.01	0.97	< 0.18	< 0.01	< 0.05	0.01	< 0.01
ZK0-112-03-6	27.9	6.82	< 0.58	60.5	< 1.52	< 62.09	< 0.50	< 2.54	< 0.06	< 0.01	1.21	0.24	0.01	< 0.02	< 0.06	< 0.01
ZK0-112-03-7	27.0	8.14	1.32	82.9	1.96	< 61.08	< 0.45	< 2.75	< 0.07	0.03	1.17	< 0.18	0.07	< 0.05	0.06	< 0.01
ZK0-112-03-8	32.3	4.66	< 0.96	48.1	< 1.90	< 87.81	< 0.43	< 2.98	< 0.12	< 0.02	1.16	< 0.41	< 0.01	< 0.06	< 0.05	0.01
ZK0-112-03-9	31.4	5.73	< 0.98	55.9	< 1.80	< 74.34	< 0.31	< 1.87	< 0.08	0.01	0.82	< 0.20	0.01	< 0.05	< 0.05	< 0.01
ZK0-112-03-10	32.6	3.61	1.29	49.9	< 1.75	< 62.31	< 0.33	< 1.99	0.09	< 0.02	1.10	< 0.22	0.01	< 0.05	0.03	< 0.01
ZK0-112-03-11	36.3	2.85	2.68	49.9	< 3.88	< 86.08	< 0.44	< 3.75	3.10	< 0.05	0.95	< 0.46	0.03	< 0.07	< 0.05	0.17
ZK0-112-03-12	29.3	3.06	< 0.98	63.4	< 1.59	< 55.22	< 0.29	< 1.71	2.59	< 0.03	1.14	< 0.24	< 0.01	< 0.04	< 0.05	< 0.01
ZK0-112-03-13	25.0	6.78	4.34	97.5	5.13	< 67.27	< 0.53	< 2.98	< 0.15	< 0.04	0.82	< 0.28	0.12	< 0.05	< 0.08	0.02
ZK15-104-04-1	6.50	2.00	< 0.87	29.3	< 0.85	< 38.39	< 0.89	< 1.68	0.20	0.01	1.97	0.19	< 0.01	0.05	< 0.02	0.01
ZK15-104-04-2	5.65	1.04	< 0.75	23.0	< 0.73	< 50.34	< 1.03	< 2.13	< 0.15	< 0.01	1.58	0.18	< 0.01	< 0.02	< 0.02	0.01
ZK15-104-04-3	16.0	3.39	< 0.65	35.8	< 0.82	< 34.29	< 0.83	< 1.66	< 0.16	0.01	1.89	0.15	< 0.01	< 0.03	< 0.02	< 0.01
ZK15-104-04-4	21.4	7.77	1.14	105	3.79	< 26.91	< 0.79	< 1.60	< 0.16	< 0.01	1.98	0.14	0.03	0.04	0.04	0.01
ZK15-104-04-5	24.2	5.79	< 0.68	95.3	2.01	< 37.07	< 0.75	< 1.72	< 0.13	0.01	1.90	< 0.09	0.02	0.03	0.04	0.01
ZK15-104-04-6	19.5	12.5	< 0.60	177	< 0.63	< 34.18	< 0.93	< 1.72	0.17	< 0.01	3.23	0.14	< 0.01	0.20	< 0.02	< 0.01
ZK15-104-04-7	26.5	17.1	0.69	243	< 0.57	< 27.63	< 1.00	< 1.68	< 0.17	< 0.01	3.85	0.24	< 0.01	0.47	0.01	< 0.01
ZK15-104-04-8	7.74	3.20	< 0.82	42.7	< 0.61	< 40.96	< 0.79	< 1.45	< 0.14	< 0.01	2.32	0.19	< 0.01	0.04	< 0.03	< 0.01
ZK15-104-04-9	5.40	3.99	< 0.78	38.2	< 0.64	< 34.68	< 0.83	< 1.71	< 0.11	< 0.01	1.84	0.16	< 0.01	< 0.02	0.01	< 0.01
ZK15-104-04-10	10.5	4.51	< 0.83	45.5	< 0.53	< 35.55	< 0.92	< 1.73	< 0.11	< 0.02	1.70	0.10	< 0.01	< 0.02	< 0.03	< 0.01
ZK15-104-04-11	2.91	1.48	< 0.74	14.2	< 0.65	< 43.85	< 1.02	< 1.49	< 0.16	< 0.01	1.97	< 0.15	< 0.01	< 0.04	< 0.03	< 0.01
ZK15-104-04-12	9.16	5.83	< 0.72	56.5	< 0.62	< 39.61	< 0.91	< 1.79	< 0.12	< 0.02	2.47	0.17	< 0.01	0.05	< 0.03	< 0.01
ZK15-104-04-13	5.75	3.60	< 0.60	33.1	< 0.59	< 36.68	0.91	< 1.53	< 0.12	< 0.01	1.95	0.15	< 0.01	0.03	< 0.03	< 0.01
ZK15-104-04-14	4.70	1.54	< 0.67	17.1	< 0.57	< 29.43	< 0.82	< 1.56	< 0.14	0.01	1.60	< 0.12	< 0.06	< 0.03	< 0.03	< 0.01
ZK15-104-04-15	8.37	1.95	< 0.82	29.6	< 0.62	< 38.41	< 0.95	< 1.58	< 0.12	< 0.01	1.59	0.18	< 0.01	< 0.03	< 0.03	< 0.01

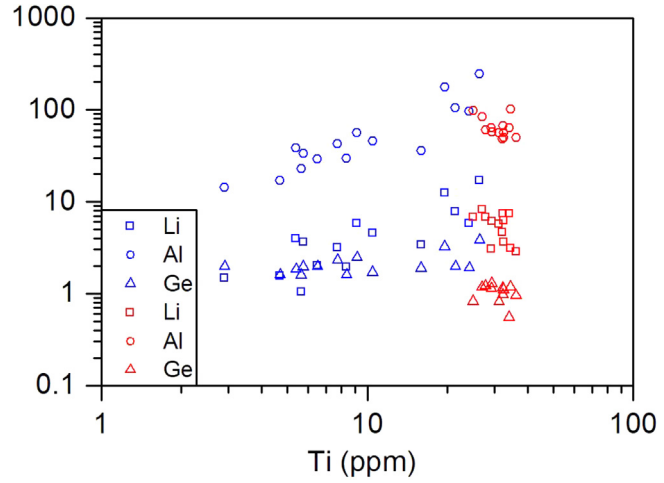

Fig. 11. Trace element concentrations in quartz. Red symbols stand for sample ZK0-112-03, and blue symbols refer to sample ZK15-104-04. (For interpretation of the references to color in this figure legend, the reader is referred to the web version of this article.)

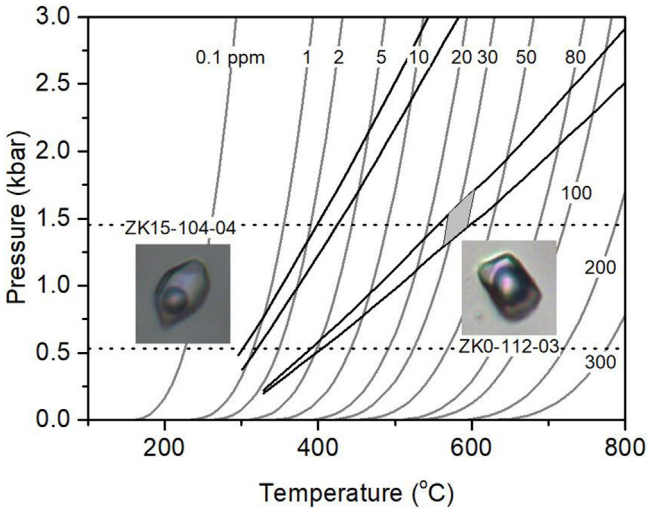

Fig. 13. Pressure and temperature diagram showing the formation conditions for quartz-bearing veins in the Yuanzhuding porphyry deposit. Gray curves are Ti-isopleths calculated from Eq. (2) (Huang and Audétat, 2012). Labelled values on gray curves are the corresponding Ti contents in quartz. Black solid line are isochores calculated from fluid inclusions from sample ZK0-112-03 and ZK15-104-04. Black dash lines are the inferred pressure values for fluid inclusion entrapment.

The application of the above Ti-in-biotite geothermometer to the hydrothermal biotite may lead to improper values because the geothermometer was originally calibrated for metapelites. However, the intrinsic correlations between crystallization temperature and biotite compositions (Ti concentration and X_{Mg} ratios) are universal for biotite formed in the same condition. Therefore, instead of reporting absolute temperatures of biotite crystallization with the above geothermometer, we calculated the temperature ratios for Bt-III from each drill hole by comparing the calculated temperatures with that in drill hole ZK0-112. The temperature ratios of Bt-III decrease from ~1.0 in drill hole ZK0-112 to ~0.89 in drill hole ZK11-112 to ~0.85 in drill hole ZK15-104 which is furthest from the center of the porphyry. The decreasing ratios with increasing distance from the porphyry center therefore support the above observation of the cooling of the ore-forming fluid during its outward migration from the porphyry into the Upper Cambrian Shuikou Group metasandstone.

5.4. Pressure and temperature conditions of the hydrothermal fluid

Many of the early quartz-bearing veins in the Yuanzhuding porphyry deposit typically show irregular vein walls and are characterized

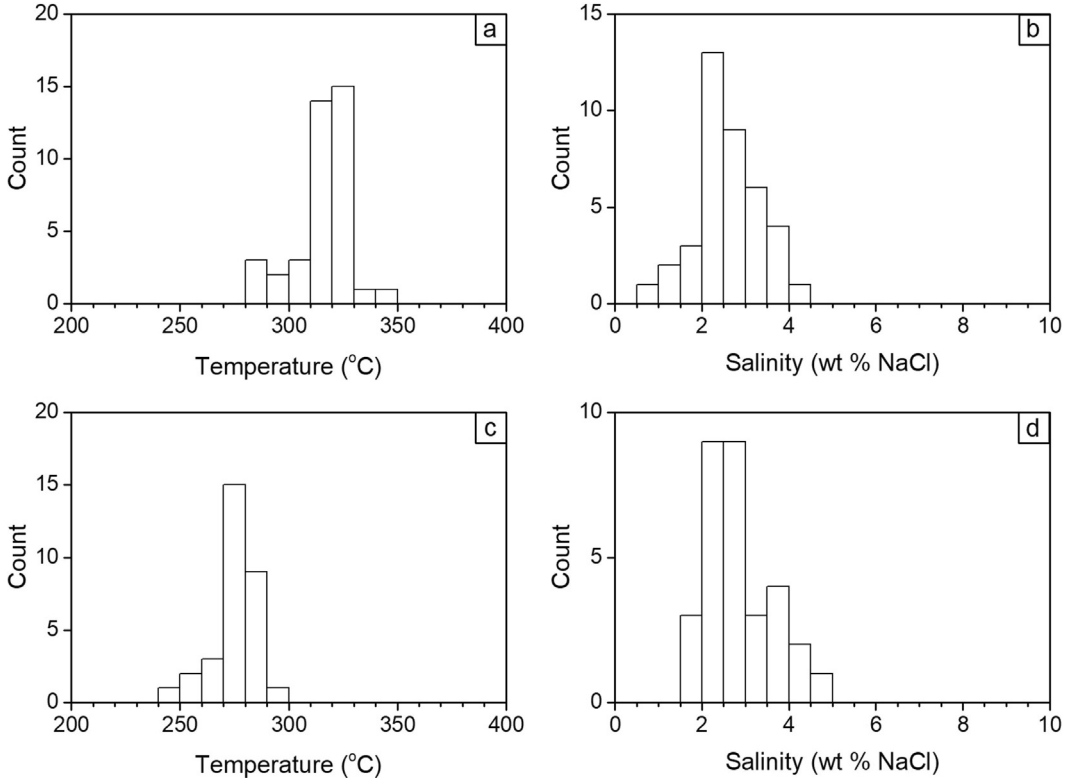

Fig. 12. Histograms of fluid inclusion homogenization temperature and fluid salinity. a, b form sample K0-112-03. c, d from sample ZK15-104-04.

Table 3
Microthermometry of fluid inclusions in the Yuanzhuding porphyry Cu-Mo deposit.

Sample	NO. of analysis	Inclusion type	Bubble volume range (%)	Ice melting temperature (°C)	Solid CO_2 melting temperature (°C)	Clathrate melting temperature (°C)	Homogenization temperature range (°C)	Salinity (wt % NaCl)	Mol % of CO_2	Density (g/cm^3)
ZK0-112-03	39	V + L	40–55	−2.5 to −5.8 avg = −4.4	−56.8 to −56.6	7.9–9.6 avg = 8.7	284–343 avg = 316	0.8–4.1 avg = 2.5	2.2–3.2 avg = 2.6	0.50–0.65 avg = 0.60
ZK15-104-04	31	V + L	15–30	−3.1 to −5.3 avg = −4.5	−56.9 to −56.6	7.6–9.2 avg = 8.6	248–295 avg = 275	1.6–4.7 avg = 2.8	1.7–2.0 avg = 1.8	0.74–0.83 avg = 0.78

by homogeneous granular mosaic CL textures (Fig. 10a, b, c). Mao et al. (2017) inferred that this type of veins was formed under dominantly lithostatic pressure. In contrast, late quartz-bearing veins in the Yuanzhuding porphyry deposit are bounded by straight vein walls and are characterized by euhedral growth zone CL textures (Fig. 10d, e). These veins are likely formed under dominantly hydrostatic pressure conditions (Mao et al., 2017).

The fluid inclusions from the Yuanzhuding porphyry deposit were trapped at a fluid pressure corresponding to the one phase field. To estimate the pressure and temperature of entrapment, an isochoric correction is conducted by intersecting the isochores of fluid inclusions in ZK0-112-03 with the corresponding Ti-in-quartz isopleth (Fig. 13). Rutile is presented in quartz-bearing veins in sample ZK0-112-03, therefore, a TiO_2 activity of one is assumed for the calculation of Ti-isopleths with the equation of Huang and Audétat (2012):

$$log\ Ti(ppm) = -0.27943*10^4/T - 660.53*(P^{0.53}/T) + 5.6459 \quad (2)$$

The intersection lies at temperature around 575 °C and pressure around 1.45 kbar. Under lithostatic conditions, the above pressure can be converted to a depth of ~5.3 km for the Yuanzhuding porphyry deposit, assuming rock density of 2.75 g/cm^3. Sample ZK0-112-03 is in close contact with the ore-forming intrusion. As revealed in the biotite composition, quartz-bearing veins further away from the porphyry should be formed at lower temperature than 575 °C, although the absolute temperature is not evaluated.

On one hand, the Ti-in-quartz thermobarometer was calibrated for high temperature conditions (600 to 800 °C), so the extrapolation to lower temperature conditions may lead to unacceptable errors. On the other hand, the large variations of Ti contents indicate that Ti were incorporated in quartz kinetically, so the Ti-in-quartz thermobarometer is not valid to get the pressure and temperature conditions for such quartz-bearing veins.

The current location of sample ZK15-104-04 (NO. 10 in Fig. 3) is ~400 m away from and ~100 m deeper than sample ZK0-112-03 (NO. 2 in Fig. 3). Assuming there is no significant uplift during the formation of these two generations of veins, we infer that the quartz-bearing veins in ZK15-104-04 were formed at the same depth of ~5.3 km. Under hydrostatic conditions, this depth equals to a pressure of 0.53 kbar, assuming fluid density of 1 g/cm^3. Intersection of the fluid inclusion isochores with the estimated pressure yields the temperature of ~310 °C (Fig. 13).

An exhumation and erosion of over 5 km is required for the Yuanzhuding porphyry deposit to be exposed near surface. Previous studies revealed that large areas of Mesozoic granitoids are exposed in the Cathaysia block, suggesting significant local uplift and erosion, probably greater than 10 km (Zhou et al., 2006). Tungsten (and Sn) deposits are suggested to be formed at relatively greater depth than porphyry Cu (Mo) deposits (Robb, 2005). South China hosts significant

Table 5
Calculated temperature of Bt-II and $Fe^{2+}/(Fe^{2+} + Fe^{3+})$ ratios of each biotite type.

Sample	Depth (m)	Temperature (°C)	$Fe^{2+}/(Fe^{2+}+Fe^{3+})$		
		Bt-II	Bt-I	Bt-II	Bt-III
ZK0-112-05b	95	620	0.78	0.88	0.94
ZK0-112-03	112	540		0.91	0.82
ZK0-112-02	125		0.76		0.87
ZK0-112-01	136		0.66		
ZK0-112-08	168	570		0.90	
ZK11-112-24	54				
ZK11-112-21	70	560		0.93	0.96
ZK11-112-17	158		0.79		0.96
ZK11-112-07	175				
ZK11-112-02	195				
ZK15-104-04	248				0.90
ZK22-106-09a	98				
ZK26-100-05a	314	460		0.94	

Table 4
Hydrogen and oxygen isotopes of biotite and quartz in the Yuanzhuding porphyry Cu-Mo deposit.

Sample	Vein	Mineral	δD-Mineral	$\delta^{18}O$-Mineral	δD-H_2O	$\delta^{18}O$-H_2O
ZK0-112-02	Qz-Kf-Bt vein	Bt	−85.2	7.0	−52.8	9.5
ZK11-112-02	Qz-Kf-Bt vein	Bt	−90.2	6.9	−57.8	9.4
ZK11-112-16	Qz-Kf-Bt vein	Bt	−93.0	6.5	−60.6	9.0
ZK0-112-02	Qz-Kf-Bt vein	Qz		9.4	−55.3	8.1
ZK0-112-03	Qz-Kf-Bt vein	Qz		9.4	−55.2	8.1
ZK0-112-07	Qz-Kf-Bt vein	Qz		9.3	−52.4	8.0
ZK11-112-02	Qz-Kf-Bt vein	Qz		9.5	−59.4	8.2
ZK11-112-07	Qz-Kf-Bt vein	Qz		11.5	−67.9	10.2
ZK11-112-16	Qz-Kf-Bt vein	Qz		10.3	−64.9	9.0
ZK15-104-04	Qz-Ser vein	Qz		11.9	−64.0	5.4
ZK22-106-06	Qz-Ser vein	Qz		13.4	−64.2	6.9
ZK26-100-03	Qz-Ser vein	Qz		10.5	−70.3	4.0

Notes: 1. The $\delta^{18}O$-δD of water was calculated with fluid temperature of 575 °C for potassic alteration and 310 °C for sericitic alteration. 2. The equation of Clayton et al. (1972) was used for the calculation of $\delta^{18}O$-H_2O with quartz and the equation of Zheng and Chen (2000) was used for the calculation of $\delta^{18}O$-H_2O with biotite. 3. The equation of Suzuoki and Epstein (1976) was used for the calculation of δD-H_2O with biotite. 4. Qz = quartz, Kf = K-feldspar, Bt = Biotite, Ser = Sericite.

amount of Mesozoic W (Sn) deposits that were formed at great depth and uplifted to near surface depths (e.g., Wang et al., 2007; Xi et al., 2008). The Mid-Jurassic Dabaoshan porphyry Mo deposit located in north Guangdong Province was estimated to be formed at 6 to 7 km (Mao et al., 2017). All the above evidences suggest that South China has experienced significant local uplift after the Mesozoic and many of the shallow porphyry deposits may have been eroded, but the deeper deposits are exposed to near the current surface.

5.5. Oxidation state variation and metal precipitation mechanism

Ferric and ferrous iron can be reasonably estimated by stoichiometric calculation in biotite (Ludington and Munoz, 1975; Dymek, 1983; Yavuz and Öztas, 1997). Considering the octahedral vacancies related to the potential Ti-substitution and Al-substitution, Dymek (1983) proposed a normalization equation for the estimation of iron oxidation state:

$$\text{Total cations}-(K + Na + Ca + Ba) + Ti + 0.5Al^{IV}{}_{xc} = 7.0 \quad (3)$$

where

$$Al^{IV}{}_{xc} = (Al + Cr)^{VI} - Al^{IV} + (K + Na + 2Ca + 2Ba)$$

Normalization of biotite EMPA data based on equation (3) therefore eliminates the calculated charge excess and presents proper estimation of Fe^{3+} content.

Annite, the iron end member of biotite, has a chemical formula of $KFe_3{}^{2+}AlSi_3O_{10}(OH)_2$ where ferrous iron is dominant (Rieder et al., 1998). Ferric iron is more available at higher oxidation conditions to substitute ferrous iron and form "oxyannite" (Wones and Eugster, 1965). Therefore, we infer that the smaller $Fe^{2+}/(Fe^{2+} + Fe^{3+})$ ratios of biotite indicate higher oxidation condition. Bt-I has the lowest $Fe^{2+}/(Fe^{2+} + Fe^{3+})$ ratio of ~0.75 of all three types of biotite, indicating that the magmatic system has the highest oxidation state (Table 5). Bt-II has a much higher average $Fe^{2+}/(Fe^{2+} + Fe^{3+})$ ratio of ~0.91 compared to Bt-I. The lowest $Fe^{2+}/(Fe^{2+} + Fe^{3+})$ ratio in Bt-II recorded in ZK0-112-05b (~0.88) is likely related to its intimate contact with the granite porphyry, indicating the impact of the oxidized intrusion to the metasandstone of reduced oxidation state. Bt-II in sample ZK26-100-05a has the highest average $Fe^{2+}/(Fe^{2+} + Fe^{3+})$ ratio of ~0.94, possibly owing to its most distal location to the porphyry. Bt-III has an average $Fe^{2+}/(Fe^{2+} + Fe^{3+})$ ratio of ~0.91, similar to that of Bt-II. Average $Fe^{2+}/(Fe^{2+} + Fe^{3+})$ ratio of Bt-III hosted in ZK0-112 of ~0.88 is smaller than that in drill holes further away from the porphyry center. Therefore, we infer that the hydrothermal fluid experienced a decrease in oxidation state during its outward migration and the interaction with the hornfels.

The generation of reduced S^{2-} in the relatively oxidized hydrothermal fluid is one of the key factors to cause metal precipitation as sulfides (Seedorff et al., 2005; Sillitoe, 2010; Sun et al., 2013). Ohmoto and Goldhaber (1997) inferred that the disproportionation reaction ($4SO_2 + 4H_2O \rightarrow 3HSO_4^- + 3H^+ + H_2S$) is the most important mechanism for the generation of reduced S^{2-}. However, the disproportionation reaction is only effective at temperatures ≤400 °C (Henley et al., 2015).

Significant Cu and Mo mineralization occurred in the high-temperature potassic alteration stage in the Yuanzhuding deposit (Figs. 3, 4). Isochoric correction indicates that fluid temperature was up to ~575 °C in sample ZK0-112-03 in which chalcopyrite and molybdenite are deposited (Fig. 10a, b, c). The disproportionation reaction is not fully capable of addressing metal precipitation at the high temperature stage in the Yuanzhuding porphyry deposit. Henley et al. (2015) inferred that the chemisorption reaction between SO_2 in fluid and the plagioclase ($3CaAl_2Si_2O_8 + 4SO_2 + H_2O \rightarrow 3CaSO_4 + 3Al_2SiO_5 + 3SiO_2 + H_2S$) is the trigger for high temperature mineralization in hydrothermal deposits. In addition to sulfur, other elements with variable oxidation states and sufficient abundance to affect the redox state of the upper crust include C, H, and Fe (Mungall, 2002). As carbon and hydrogen are dominantly presented as CO_2 and H_2O in the oxidized porphyry system, ferrous iron therefore serves as an important reducing agent (Sun et al., 2013).

The abundant Bt-II in hornfels around the Yuanzhuding granite porphyry hosts significant amount of ferrous iron. The close spatial distribution between the altered biotite and the sulfides both in the potassic alteration zone and the sericitic alteration zone indicates their genetic relationship (Figs. 4, 5). We infer that the hornfels (as well as the Shuikou Group metasandstone) served as a reservoir of ferrous iron and provide the capability of reducing the SO_2 in the ore-forming fluid to S^{2-}. In addition to the drop of metal solubility caused by the decrease of temperature, the hydrothermal fluid therefore unloaded the metals as sulfides in the host rock around the porphyry.

5.6. Halogen fugacity and comparison with other porphyry deposits

To evaluate the F = OH and Cl = OH exchange in the hydroxyl site (A site) in biotite, Munoz (1984) defined the fluorine and chlorine intercept-values for biotite as follows:

$$IV(F) = 1.52X_{Mg} + 0.42X_{An} + 0.20X_{Sid} - \log(X_F/X_{OH}) \quad (4)$$

$$IV(Cl) = -5.01 - 1.93X_{Mg} - \log(X_{Cl}/X_{OH}) \quad (5)$$

$$IV(F/Cl) = IV(F) - IV(Cl) \quad (6)$$

where X_{Mg} = Mg/total octahedral cations; $X_{An} = 1 - X_{Mg} - X_{Sid}$; $X_{Sid} = [(3 - Si/Al)/1.75](1 - X_{Mg})$

X_{Mg} is the mole fraction of phlogopite; X_{An} is the mole fraction of annite; X_{Sid} is the mole fraction of siderophyllite. X_F, X_{Cl}, and X_{OH} are the mole fractions of F, Cl, and OH in the hydroxyl site, respectively. Therefore, the smaller the IV(F) values, the higher the fluorine enrichment. The higher the negative numbers of IV(Cl), the higher degree of chlorine enrichment. The lower IV(F/Cl) values correspond to higher F/Cl ratios (Munoz 1984).

Calculated IV(F) values are on average ~2.22 for Bt-I, ~2.33 for Bt-II, and ~2.17 for Bt-III (Fig. 14a). Calculated IV(Cl) values are on average around -3.57 for Bt-I, -3.48 for Bt-II, and -3.36 for Bt-III (Fig. 14b). The IV(F/Cl) values are on average ~5.79 for Bt-I, ~5.81 for Bt-II, and ~5.53 for Bt-III (Fig. 14c). Bt-II formed during the contact metamorphism and has the largest variation, likely related to the inhomogeneous property of the Upper Cambrian Shuikou Group metasandstone. Bt-III in the Yuanzhuding porphyry Cu-Mo deposit shows smaller chlorine enrichment, but comparable fluorine enrichment, in respect to other porphyry Cu deposits (Fig. 14).

Munoz (1992) presented the following equations for the evaluation of the halogen fugacity in the hydrothermal fluid with fluorine and chlorine contents in biotite:

$$\log(fH_2O/fHF)^{fluid} = 1000/T(2.37 + 1.1X_{Mg}) + 0.43 - \log(X_F/X_{OH}) \quad (7)$$

$$\log(fH_2O/fHCl)^{fluid} = 1000/T(1.15 + 0.55X_{Mg}) + 0.68 - \log(X_{Cl}/X_{OH}) \quad (8)$$

$$\log(fHF/fHCl)^{fluid} = -1000/T(1.22 + 1.65X_{Mg}) + 0.25 + \log(X_F/X_{Cl}) \quad (9)$$

where T is temperature in Kelvin.

Temperature of 575 °C acquired from ZK0-112-03 was used for the calculation of the halogen fugacities for all the Bt-III samples, despite the outward cooling trend of the Yuanzhuding hydrothermal system. Calculated $\log(fH_2O/fHF)^{fluid}$, $\log(fH_2O/fHCl)^{fluid}$, and $\log(fHF/fHCl)^{fluid}$ ratios are averagely around 5.12, 5.12, and -0.72 for the hydrothermal Bt-III in the Yuanzhuding porphyry Cu-Mo deposit.

In comparison with the Casino porphyry Cu-Au-Mo deposit, Selby and Nesbitt (2000) compiled the fugacity ratios of hydrothermal fluids in Bingham (Lanier et al., 1978; Parry et al., 1978; Bowman et al., 1987), Santa Rita (Jacobs and Parry, 1979), Los Pelambres, Bakircay

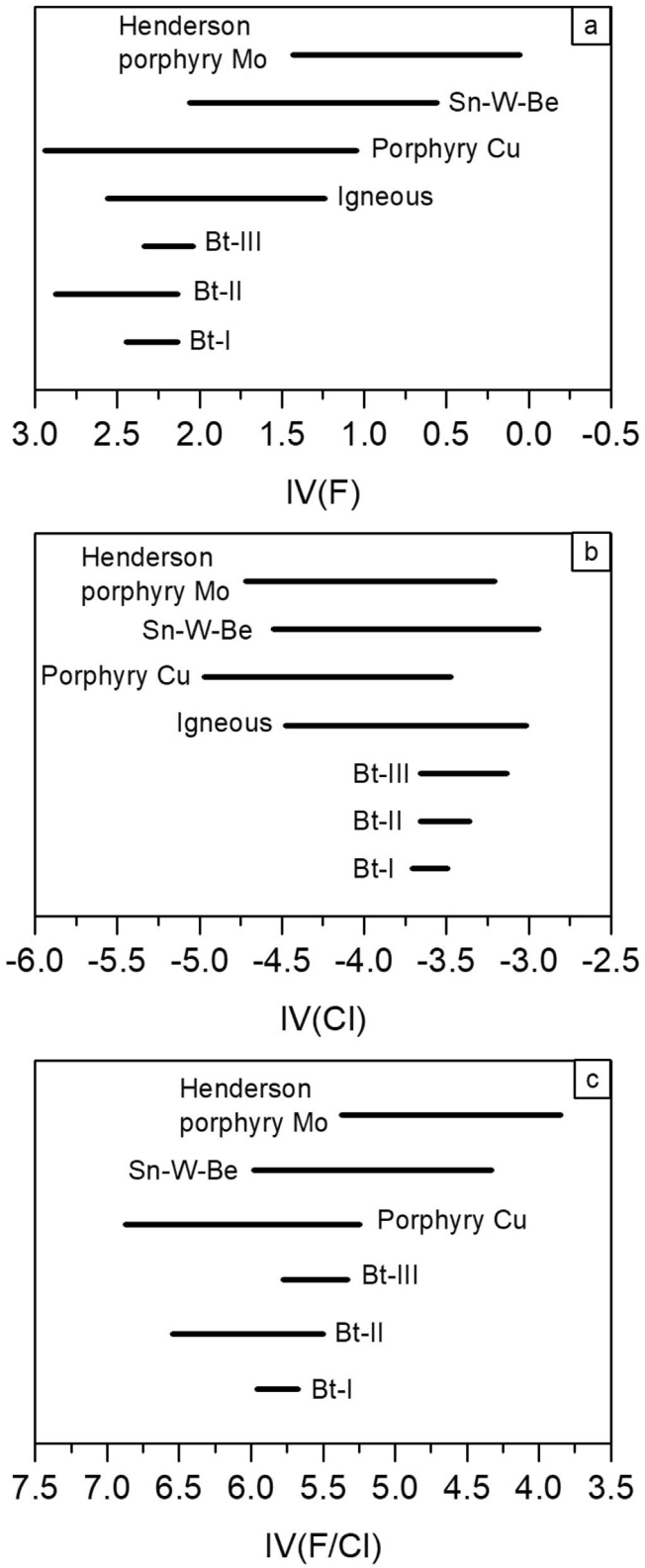

Fig. 14. Fluorine and chlorine intercept values for biotite in the Yuanzhuding porphyry deposit and comparison with other porphyry systems.

(Taylor, 1983), Babine Lake (Sheets et al., 1996), Hanover (Jacobs and Parry, 1979), and Deboullie (Loferski and Ayuso, 1995) porphyry systems. Fugacity ratios of hydrothermal fluids from six more porphyry systems including the Dalli (Ayati et al., 2008), Miduk (Boomeri et al., 2009), Sarcheshmeh (Boomeri et al., 2010), Kahang (Afshooni et al., 2013), Darreh-Zar (Parsapoor et al., 2015), and Dexing (Bao et al., 2016) porphyry deposits have been added for a more comprehensive comparison (Fig. 15).

The $\log(fH_2O/fHF)^{fluid}$ ratios of the Yuanzhuding hydrothermal fluid are lower than most other porphyry systems, while the $\log(fHF/fHCl)^{fluid}$ and $\log(fH_2O/fHCl)^{fluid}$ ratios are generally higher than most other porphyry systems, indicating that the ore-forming fluid is relatively F-rich and Cl-poor (Fig. 15c, d). This is consistent with the low fluid salinity estimated by fluid inclusion microthermometry (Table 3).

Since Bt-III located further away from the intrusion may have been crystalized at lower temperature than 575 °C, we recalculated the halogen fugacity ratios at lower temperature to evaluate the influence of temperature estimation. Potassic alteration and associated mineralization occur under lithostatic conditions and require hydrofracturing of the ductile rock (Sillitoe, 2010). At temperature below 400 °C, lithostatic gives way to hydrostatic pressure (Fournier, 1999). As all the Bt-III are from the potassic alteration stage, we infer that 400 °C is the minimal temperature of hydrothermal biotite formation. The calculation temperature at 400 °C will lead to lower $\log(fHF/fHCl)^{fluid}$ ratios and higher $\log(fH_2O/fHF)^{fluid}$ and $\log(fH_2O/fHCl)^{fluid}$ ratios (Fig. 15a, b). The recalculated $\log(fH_2O/fHCl)^{fluid}$ ratios are higher than all the other porphyry deposits, confirming that ore-forming fluid in the Yuanzhuding porphyry deposit is Cl-poor.

5.7. Origin of the ore-forming fluid

The δD and $\delta^{18}O$ values of the ore-forming fluid in the Yuanzhuding porphyry system have been acquired from the hydrogen and oxygen isotopes of hydrothermal biotite (Bt-III) and quartz (Table 4). Hydrothermal fluid hosted in fluid inclusions in quartz yielded the δD values of ~-59.2‰ in veins with potassic alteration and decrease to ~-67.3‰ in veins with sericitic alteration. Crystallization in the magma chamber will lead to the decrease of the δD values of the exsolved hydrothermal fluid (Shinohara and Hedenquist, 1997), therefore may account for the decrease of the δD values of the ore-forming fluid in the Yuanzhuding porphyry system. The calculated δD values of fluid from biotite (average ~-57.1‰) are generally consistent to that preserved in fluid inclusions in quartz.

The calculated $\delta^{18}O$ values of fluid from quartz decrease from on average ~8.6‰ in veins with potassic alteration to ~5.4‰ in veins with sericitic alteration. The average $\delta^{18}O$ value of fluid calculated from biotite is ~9.3‰. All the δD and $\delta^{18}O$ values of the hydrothermal fluid plot within or very close to the region of magmatic water (Fig. 16), indicating that the ore-forming fluid in the Yuanzhuding porphyry system has mainly originated from the magma and experienced minimal contribution from meteoric water. We infer that the lack of notable meteoric water supports the great depth of formation at ~5.3 km.

5.8. Implications for metal enrichment

Phase separation is inferred to be a significant trigger for metal enrichment and mineralization in porphyry systems (Heinrichet al., 1999; Ulrich et al., 2001; Harris et al., 2003). However, the halite-bearing and vapor-rich fluid inclusions are absent in the Yuanzhuding porphyry deposit, indicating that the ore-forming fluid had not experienced phase separation. Fluid inclusions in both the potassic alteration stage and the sericitic alteration stage are dominantly vapor-liquid fluid inclusions that homogenized to liquid. Fluid salinity varies very slightly during the whole fluid evolution history, and it is averagely ~2.5 wt% in quartz-bearing veins formed under lithostatic conditions and ~2.8 wt% in quartz-bearing veins formed under hydrostatic conditions. Vapor portion of fluid inclusions decreases from ~45 to 50 vol% in the potassic alteration stage to ~25 vol% in the sericitic alteration stage. Average fluid density, on the contrary, increases from 0.60 g/cm^3 to 0.78 g/cm^3 from early to late stage, corresponding to

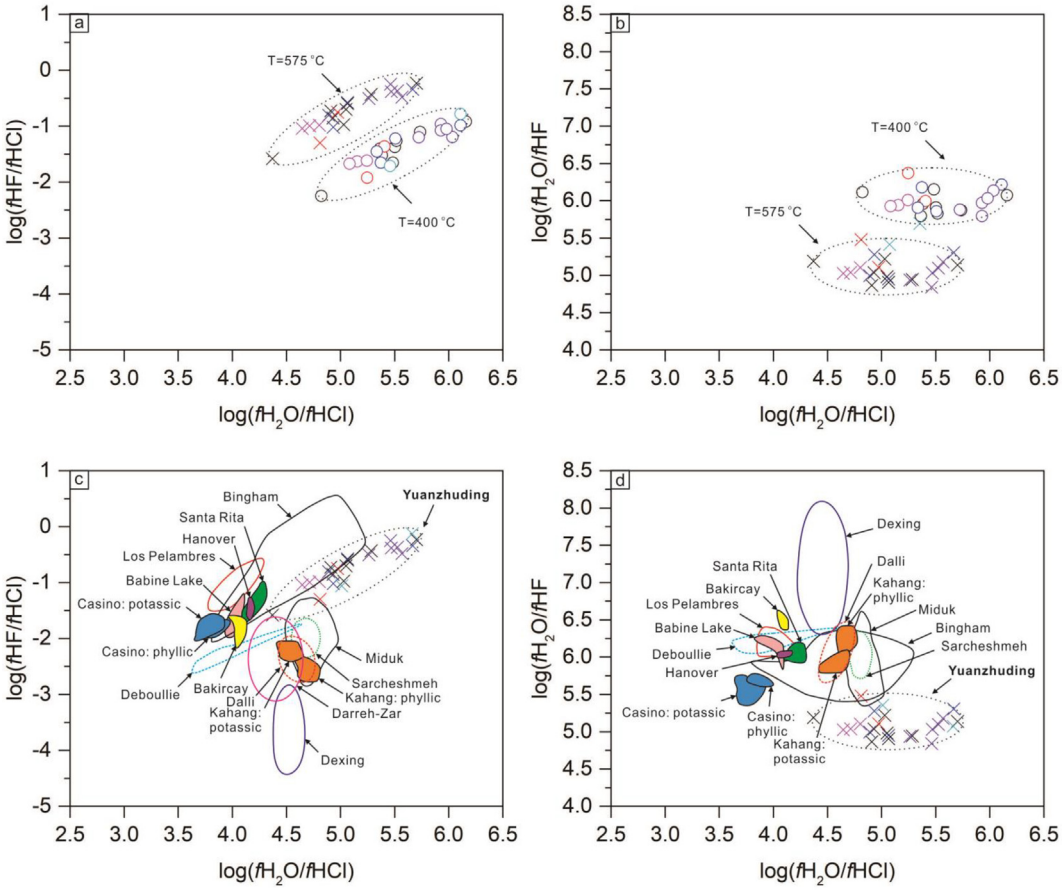

Fig. 15. Halogen fugacity diagrams for hydrothermal fluid in the Yuanzhuding porphyry deposit and the comparison with other porphyry systems. Crosses are calculated with temperature of 575 °C and circles are acquired with the temperature of 400 °C. See detailed legends in Fig. 7. Data of other deposits are collected from Bingham (Lanier et al., 1978; Parry et al., 1978; Bowman et al., 1987), Santa Rita (Jacobs and Parry, 1979), Hanover (Jacobs and Parry, 1979), Los Pelambres, Bakircay (Taylor, 1983), Deboullie (Loferski and Ayuso, 1995), Babine Lake (Sheets et al., 1996), Dalli (Ayati et al., 2008), Miduk (Boomeri et al., 2009), Sarcheshmeh (Boomeri et al., 2010), Kahang (Afshooni et al., 2013), Darreh-Zar (Parsapoor et al., 2015), and Dexing (Bao et al., 2016).

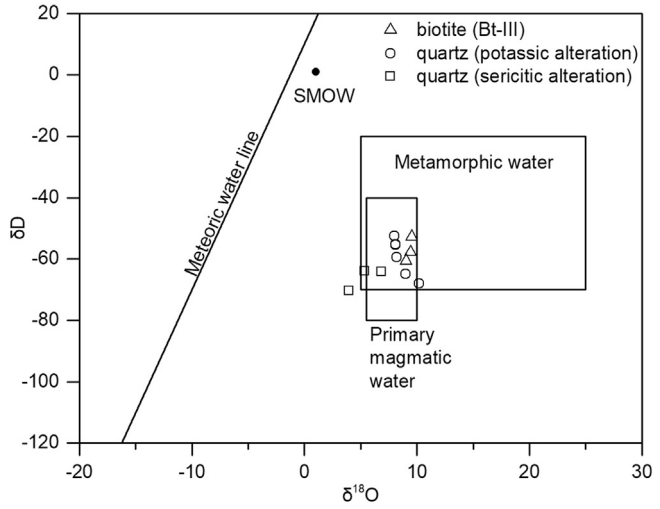

Fig. 16. $\delta^{18}O$ and δD fluid compositions calculated from quartz and hydrothermal biotite (Bt-III) in the Yuanzhuding porphyry system. See Table 4 for calculation details.

their different forming conditions.

Fugacity ratios of the hydrothermal fluid calculated from the biotite F and Cl contents clearly indicate that the ore-forming fluid in the Yuanzhuding porphyry Cu-Mo deposit is Cl-poor compared to other porphyry systems. This is also well documented in the IV(F), IV(Cl), and IV(F/Cl) values of the hydrothermal biotite (Bt-III in Fig. 14). The low Cl fugacity is consistent with the very low fluid salinity revealed by fluid inclusion microthermometry (Table 3). In contrast, the Dexing giant porphyry Cu-Mo-Au deposit, located in the northeast section of the Qinzhou-Hangzhou belt (Fig. 1a), has distinctively higher fluid Cl fugacity and lower fluid F fugacity compared to the Yuanzhuding porphyry system. The Dexing porphyry system experienced significant phase separation and fluid salinity can be as high as ~70 wt% NaCl equiv. (Zhang et al., 2012).

During the exsolution of magmatic fluid from the melt in the magma chamber, the partition coefficient of Cu between the fluid phase and the melt increases with the increase of Cl content in fluid, whereas the Mo partition coefficient is not affected (Candela and Holland 1984). Therefore, the higher Cl content of fluid indicates more effective extraction of Cu from the melt. Chlorine complexes were inferred to be the most important way of transporting Cu in the hydrothermal fluid (Candela and Holland, 1984, 1986; Cline and Bodnar, 1991; Herzarkhani et al., 1999; Harris et al., 2003; Candela and Piccoli, 2005; Audétat et al., 2008). Therefore, the high Cl content in the ore-forming fluid is one of the key factors for the formation of giant porphyry Cu systems.

The Yuanzhuding porphyry Cu-Mo deposit and the Dexing porphyry Cu-Mo-Au deposit are situated along the same metallogenic belt related to the Mid- to Late-Jurassic westward subduction of the Paleo-Pacific plate. These ore-forming porphyries are all high-K calc-alkaline granites with high Sr/Y signatures (Mao et al., 2009; Zhong et al., 2013). The ore bodies are dominantly hosted in the *meta*-sedimentary rock in both

deposits. However, the Dexing porphyry Cu-Mo-Au deposit host a total of 8.37 Mt Cu, 0.296 Mt Mo, 215 t Au, and 1279 t Ag (Mao et al., 2011a), whereas the Yuanzhuding porphyry Cu-Mo deposit hosts much less Cu resource (0.98 Mt) but comparable Mo resource (0.26 Mt).

Porphyry deposits are the products of complicated magmatic-hydrothermal evolutions, so many physical-chemical conditions may lead to the above differences in metal resources between these two deposits. For example, the sources of the ore-forming porphyries may significantly control the metal associations in porphyry deposits (Seedorff et al., 2005; Sillitoe, 2010; Sun et al., 2013). Nevertheless, we infer that the low content of Cl in the ore-forming fluid could reduce the efficiency of Cu extraction and transportation in the Yuanzhuding magmatic-hydrothermal system. It is likely one of the possible reasons that is responsible for the smaller size of Cu mineralization in the Yuanzhuding porphyry deposit, compared to the Dexing and other giant porphyry Cu deposits.

6. Conclusions

Sericite and three different generations of biotite have been identified in the Yuanzhuding porphyry Cu-Mo deposit. Igneous biotite Bt-I formed in the magmatic stage of the Yuanzhuding granite porphyry, the metamorphic biotite Bt-II formed during the contact metamorphism caused by the intrusion of the granite porphyry into the host rocks, the hydrothermal biotite Bt-III formed in the potassic alteration stage, and the hydrothermal sericite Ser formed in the sericitic alteration stage.

Fluid and crystallization temperature of the Yuanzhuding magmatic-hydrothermal systems decreases outward from the porphyry. Early quartz-bearing veins with potassic alteration located close to the ore-forming porphyry formed under lithostatic conditions at up to ~575 °C. Late quartz-bearing veins with sericitic alteration formed after the transition to hydrostatic conditions at ~310 °C. The hornfels, as well as the Shuikou Group metasandstone, likely served as a reservoir of ferrous iron to generate reduced sulfur for metal precipitation. The combination of the oxidation state reduction with the decrease of temperature caused effective metal precipitation in the Yuanzhuding porphyry Cu-Mo deposit.

The Yuanzhuding porphyry deposit was formed at ~5.3 km, which is deeper than many other porphyry deposits. H and O isotopic compositions indicate that the ore-forming fluid is predominantly of magmatic origin. It exsolved as a low-salinity, aqueous fluid from the magma and did not experienced phase separation, so the fluid salinity and the Cl fugacity remained constantly low compared to most other porphyry deposits. This may have limited the efficiency of Cu extraction from the magma chamber and Cu transportation during the hydrothermal fluid evolution, therefore, generated a smaller sized porphyry Cu deposit.

Acknowledgement

This paper is financially supported by the National Key R&D Program of China (2016YFC0600405) and the National Natural Science Foundation of China (Grant NO. 41425011, 41703049). We appreciate the assistance of Drs. Yanwen Tang, Tingguang Lan, and Juan Wang in the lab work. We acknowledge our thanks to Dr. Thomas Ulrich and the anonymous reviewer for their constructive comments, and Prof. Franco Pirajno for handling this paper.

References

Afshooni, S.Z., Mirnejad, H., Esmaeily, D., Haroni, H.A., 2013. Mineral chemistry of hydrothermal biotite from the Kahang porphyry copper deposit (NE Isfahan), Central Province of Iran. Ore Geol. Rev. 54, 214–232.
Armington, A.F., 1991. Recent advances in the growth of high quality quartz: Progress in Crystal Growth and Characterization of Materials 21 (1–4), 97–111.
Armington, A.F., Larkin, J.J., 1985. The Growth of High-Purity. Low Dislocation Quartz: J. Crystal Growth 71 (3), 799–802.
Audétat, A., Pettke, T., Heinrich, C.A., Bodnar, R.J., 2008. Special Paper: the composition of magmatic-hydrothermal fluids in barren and mineralized intrusions. Econ. Geol. 103, 877–908.
Ayati, F., Yavuz, F., Noghreyan, M., Haroni, H.A., Yavuz, R., 2008. Chemical characteristics and composition of hydrothermal biotite from the Dalli porphyry copper prospect, Arak, central province of Iran. Mineral. Petrol. 94, 107–122.
Bakker, R.J., 1997. Clathrates: computer programs to calculate fluid inclusion V-X properties using clathrate melting temperatures. Comput. Geosci. 21, 1–18.
Bao, B., Webster, J.D., Zhang, D.H., Goldoff, B.A., Zhang, R.Z., 2016. Compositions of biotite, amphibole, apatite and silicate melt inclusions from the Tongchang mine, Dexing porphyry deposit, SE China: Implications for the behavior of halogens in mineralized porphyry systems. Ore Geol. Rev. 79, 443–462.
Bowers, T.S., Hegeson, H.C., 1983. Calculation of the thermodynamic and geochemical consequences of nonideal mixing in the system H_2O-CO_2-NaCl on phase relations in geologic systems. Am. Mineral. 68, 1059–1075.
Beane, R.E., 1974. Biotite stability in the porphyry copper environment. Econ. Geol. 69, 241–256.
Boomeri, M., Nakashima, M., Lentz, D.R., 2009. The Miduk porphyry Cu deposit, Kerman, Iran: a geochemical analysis of the potassic zone including halogen element systematics related to Cu mineralization processes. J. Geochem. Explor. 103, 17–29.
Boomeri, M., Nakashima, M., Lentz, D.R., 2010. The Sarcheshmeh porphyry copper deposit, Kerman, Iran: amineralogical analysis of the igneous rocks and alteration zones including halogen element systematics related to Cu mineralization processes. Ore Geol. Rev. 38, 367–381.
Bowman, J.R., Parry, W.T., Kropp, W.P., Kruer, S.A., 1987. Chemical and isotopic evolution of hydrothermal solutions at Bingham. Utah. Econ. Geol. 82, 395–428.
Breiter, K., Ackerman, L., Svojtka, M., Müller, A., 2013. Behavior of trace elements in quartz from plutons of different geochemical signature: a case study from the Bohemian Massif, Czech Republic. Lithos 175–176, 54–67.
Candela, P.A., Holland, H.D., 1984. The partitioning of copper and molybdenum between silicate melts and aqueous fluids. Geochim. Cosmochim. Acta 48, 373–380.
Candela, P.A., Holland, H.D., 1986. A mass transfer model for copper and molybdenum in magmatic hydrothermal systems: the origin of porphyry-type ore deposits. Econ. Geol. 81, 1–19.
Candela, P.A., Piccoli, P.M., 2005. Magmatic processes in the development of porphyry-type ore systems. Economic Geology 100th Anniversary Volume. pp. 25–37.
Chen, L., Liu, Y., Hu, Z., Gao, S., Zong, K., Chen, H., 2011. Accurate determinations of fifty-four major and trace elements in carbonate by LA-ICP-MS using normalization strategy of bulk components as 100%. Chem. Geol. 284 (3–4), 283–295.
Chu, K.L., 2013. The Diagenesis and Metallogenesis studies on Yuanzhuding porphyry Cu-Mo deposit in Guangdong. Dissertation, Chinese Academy of Geological Sciences (in Chinese with English abstract).
Clayton, R.N., Mayeda, T.K., Oneil, J.R., 1972. Oxygen isotope-exchange between quartz and water. J. Geophys. Res. 77, 3057–3067.
Clayton, W.M., Mayeda, T.K., 1963. The use of bromine pent a fluoride in the extraction of oxygen from oxides and silicates for isotopic analysis. Geochim. Cosmochim. Acta 27, 43–52.
Cline, J.S., Bodnar, R.J., 1991. Can economic porphyry copper mineralization be generated by a typical calc-alkaline melt? J. Geophys. Res. 96, 8113–8126.
Coulson, I.M., Dipple, G.M., Raudsepp, M., 2001. Evolution of HF and HCl activity in magmatic volatiles of the gold-mineralized Emerald Lake pluton, Yukon Territory, Canada. Mineralium Deposita 36, 594–606.
Czamanske, G.K., Wones, D.R., 1973. Oxidation during magmatic differentiation, Finnmarka Complex, Oslo area, Norway: Part 2. The mafic silicates. J. Petrol. 14 (3), 349–380.
Dilles, J.H., Einaudi, M.T., 1992. Wall-rock alteration and hydrothermal flow path about the Ann-Mason porphyry copper deposit, Nevada-A 6-km vertical reconstruction. Econ. Geol. 87, 1963–2001.
Donovan, J.J., Lowers, H.A., Rusk, B.G., 2011. Improved electron probe microanalysis of trace elements in quartz. Am. Mineral. 96, 274–282.
Duan, Z., Møller, N., Weare, J.H., 1992. An equation of state for the CH_4-CO_2-H_2O system: I. Pure systems from 0 to 1000 °C and 0 to 8000 bar. Geochim. Cosmochim. Acta 56, 2605–2617.
Duan, Z., Møller, N., Weare, J.H., 1992. An equation of state for the CH_4-CO_2-H_2O system: II. Mixtures from 50 to 1000 °C and 0 to 1000 bar. Geochim. Cosmochim. Acta 56, 2619–2631.
Dymek, R.F., 1983. Titanium, aluminum and interlayer cation substitutions in biotite from high-grade gneisses, west Greenland. Am. Mineral. 68, 880–899.
Feldstein, S.N., Lange, R.A., Vennemann, T., O'Neil, J.R., 1996. Ferric-ferrous ratios, H_2O contents and D/H ratios of phlogopite and biotite from lavas of different tectonic regimes. Contrib. Mineral. Petrol. 126, 51–66.
Fournier, R.O., 1999. Hydrothermal processes related to movement of fluid from plastic into brittle rock in the magmatic-epithermal environment. Econ. Geol. Bull. Soc. 94, 1193–1211.
Goldstein, R.H., Reynolds, T.J., 1994. Systematics of Fluid Inclusions in Diagenetic Minerals: SEPM Short Course 31. Society of Sedimentary Geology, pp. 199.
Götte, T., Pettke, T., Ramseyer, K., Koch-Müller, M., Mullis, J., 2011. Cathodoluminescence properties and trace element signature of hydrothermal quartz: a fingerprint of growth dynamics. Am. Mineral. 96, 802–813.
Götze, J., 2009. Chemistry, textures and physical properties of quartz-geological interpretation and technical application. Mineral. Mag. 73 (4) 645–671.
Götze, J., Plötze, M., Graupner, T., Hallbauer, D.K., Bray, C.J., 2004. Trace element incorporation into quartz: A combined study by ICPMS, electron spin resonance, cathodoluminescence, capillary ion analysis, and gas chromatography. Geochim. Cosmochim. Acta 68, 3741–3759.
Harris, A.C., Kamenetsky, V.S., White, N.C., van Achterbergh, E., Ryan, C.G., 2003. Melt

inclusions in veins: linking magmas and porphyry Cu deposits. Science 302, 2109–2111.
Heinrich, C.A., Günther, D., Audétat, A., Ulrich, T., Frischknecht, R., 1999. Metal fractionation between magmatic brine and vapor, determined by microanalysis of fluid inclusions. Geology 27, 755–758.
Henley, R.W., King, P.L., Wykes, J.L., Renggli, C.J., Brink, F.J., Clark, D.A., Troitzsch, U., 2015. Porphyry copper deposit formation by sub-volcanic sulphur dioxide flux and chemisorption. Nat. Geosci. 8, 210–215.
Henry, D.J., 2005. The Ti-saturation surface for low-to-medium pressure metapelitic biotites: Implications for geothermometry and Ti-substitution mechanisms. Am. Mineral. 90, 316–328.
Herzarkhani, A., Williams-Jones, A.E., Gammons, C.H., 1999. Factors controlling copper solubility and chalcopyrite deposition in the Sungun porphyry copper deposit, Iran. Mineralium Deposita 34, 770–783.
Hua, R.M., Mao, J.W., 1999. A preliminary discussion on the Mesozoic metallogenic explosion in East China. Mineral Deposits 18, 300–307.
Huang, R.F., Audétat, A., 2012. The titanium-in-quartz (TitaniQ) thermobarometer: a critical examination and re-calibration. Geochim. Cosmochim. Acta 84, 75–89.
Jacamon, F., Larsen, R.B., 2009. Trace element evolution of quartz in the charnockitic Kleivan granite, SW-Norway: the Ge/Ti ratio of quartz as an index of igneous differentiation. Lithos 107 (3–4), 281–291.
Jacobs, D.C., Parry, W.T., 1979. Geochemistry of biotite in the Santa Rita porphyry copper deposit, New Mexico. Econ. Geol. 74, 860–887.
Jochum, K.P., Weis, U., Stoll, B., Kuzmin, D., Yang, Q., Raczek, I., Jacob, D.E., Stracke, A., Birbaum, K., Frick, D.A., Günther, D., Enzweiler, J., 2011. Determination of reference values for NIST SRM 610–617 glasses following ISO guidelines. Geostandards Geoanal. Res. 35, 397–429.
Jourdan, A.-L., Vennemann, T.W., Mullis, J., Ramseyer, K., Spiers, C.J., 2009. Evidence of growth and sector zoning in hydrothermal quartz from Alpine veins Eur. J. Mineral. 21 (1), 219–231.
Lan, T.G., Hu, R.Z., Bi, X.W., Mao, G.J., Wen, B.J., Liu, L., Chen, Y.H., 2017a. Metasomatized asthenospheric mantle contributing to the generation of Cu-Mo deposits within an intracontinental setting: a case study of the ~128 Ma Wangjiazhuang Cu-Mo deposit, eastern North China Craton. J. Asian Earth Sci. 160, 460–489.
Lan, T.G., Hu, R.Z., Fan, H.R., Bi, X.W., Tang, Y.W., Zhou, L., Mao, W., Chen, Y.H., 2017b. In-situ analysis of major and trace elements in fluid inclusion and quartz: LA-ICP-MS method and applications to ore deposits. Acta Petrologica Sinica 33 (10), 3239–3262 (in Chinese with English abstract).
Landtwing, M.R., Pettke, T., 2005. Relationships between SEM-cathodoluminescence response and trace-element composition of hydrothermal vein quartz. Am. Mineral. 90, 122–131.
Lanier, G., Raab, W.J., Folsom, R.B., Cone, S., 1978. Alteration of equigranular monzonite, Bingham Mining District, Utah. Econ. Geol. 73, 1270–1286.
Larsen, R.B., Polvé, M., Juve, G., 2000. Granite pegmatite quartz from Evje-Iveland: Trace element chemistry and implications for the formation of high-purity quartz. Bull. Geol. Survey Norway. 436, 57–65.
Lehmann, K., Berger, A., Götte, T., Ramseyer, K., Wiedenbeck, M., 2009. Growth related zonations in authigenic and hydrothermal quartz characterized by SIMS-, EPMA-, SEM-CL- and SEM-CC-imaging. Mineral. Mag. 73, 633–643.
Li, X.F., Hu, R.M., Rusk, B., Xiao, R., Wang, C.Y., Yang, F., 2013. U-Pb and Ar-Ar geochronology of the Fujiawu porphyry Cu-Mo deposit, Dexing district, Southeast China: implications for magmatism, hydrothermal alteration, and mineralization. J. Asian Earth Sci. 74, 330–342.
Li, X.F., Yasushi, W., Hua, R.M., Mao, J.W., 2008. Mesozoic Cu-Mo-W-Sn Mineralization and Ridge/Triple Subduction in South China. Acta Geol. Sin. 82 (5), 625–640 (in Chinese with English abstract).
Liang, J., Zhou, Y.Z., Li, H.Z., Yin, Z.Z., Zhou, L.Y., Yin, Z.Z., 2015. A study of the regional geology and tectonic evolution in Nanhe area of Lianjiang County, Guangdong Province, in southern section of Qinzhou Bay-Hangzhou Bay Metallogenic belt. Earth Sci. Front. 22 (2), 86–94.
Liang, J., Zhou, Y.Z., Li, H.Z., Yin, Z.Z., Zhou, L.Y., Zeng, C.Y., Yu, P.P., 2012. Geological characteristics and genesis of porphyry copper deposits in Qinzhou-Hangzhou suture zone, South China. Acta Petrologica Sinica 28 (10), 3361–3372 (in Chinese with English abstract).
Lin, X.G., Gu, X.M., Wang, Y.D., 2011. Preliminary investigation of the geology and ore-forming mechanism of the Yuanzhuding porphyry Cu-Mo deposit in Fengkai, Guangdong Province. West-China Exploration Eng. 9, 208–211 (in Chinese with English abstract).
Liu, Y.S., Hu, Z.C., Gao, S., Günther, D., Xu, J., Gao, C.G., Chen, H.H., 2008. In situ analysis of major and trace elements of anhydrous minerals by LA-ICP-MS without applying an internal standard. Chem. Geol. 257 (1–2), 34–43.
Loferski, P.J., Ayuso, R.A., 1995. Petrography and mineral chemistry of the composite Deboullie pluton, northern Maine, U.S.A.: implications for the genesis of Cu-Mo mineralization. Chem. Geol. 123, 89–105.
Ludington, S., Munoz, J.L., 1975. Application of fluorhydroxyl exchange data to natural micas. Geol. Soc. Am. Abstr. Programs 7, 1179.
Mao, J.W., Chen, M.H., Yuan, S.D., Guo, C.L., 2011a. Geological characteristics of the Qinhang (or Shihang) Metallogenic Belt in South China and spatial temporal distribution regularity of mineral deposits. Acta Geol. Sin. 85 (5), 636–658 (in Chinese with English abstract).
Mao, J.W., Cheng, Y.B., Chen, M.H., Pirajno, F., 2013a. Major types and time-space distribution of Mesozoic ore deposits in South China and their geodynamic settings. Miner. Deposita 48, 267–294.
Mao, J.W., Pirajno, F., Lehmann, B., Luo, M., Berzina, A., 2014. Distribution of porphyry deposits in the Eurasian continent and their corresponding tectonic settings. J. Asian Earth Sci. 79, 576–584.
Mao, J.W., Xie, G.Q., Cheng, Y.B., Chen, Y.C., 2009. Mineral deposit models of Mesozoic ore deposits in South China. Geol. Rev. 55, 347–354.
Mao, J.W., Xie, G.Q., Duan, C., Pirajno, F., Ishiyama, D., Chen, Y.C., 2011b. A tectonogenetic model for porphyry-skarn-stratabound Cu-Au-Mo-Fe and magnetite-apatite deposits along the Middle-Lower Yangtze River Valley, Eastern China. Ore Geol. Rev. 43, 294–314.
Mao, J.W., Xie, G.Q., Guo, C.L., Yuan, S.D., Cheng, Y.B., Chen, Y.C., 2008. Spatial-temporal distribution of Mesozoic ore deposits in South China and their metallogenic settings. Geol. J. China Univ. 510–526 (in Chinese with English abstract).
Mao, J.W., Xie, G.Q., Li, X.F., Zhang, C.Q., Mei, Y.X., 2004. Mesozoic large scale mineralization and multiple lithospheric extension in South China. Earth Sci. Front. 1, 45–55 (in Chinese with English abstract).
Mao, W., Li, X., Yang, F., 2013b. Zircon LA-ICP-MS U-Pb ages of granites at Dabaoshan polymetallic deposit and its geological significance, Guangdong, South China. Acta Petrologica Sinica 29, 4104–4120 (in Chinese with English abstract).
Mao, W., Rusk, B., Yang, F., Zhang, M., 2017. Physical and chemical evolution of the Dabaoshan porphyry Mo deposit, South China: Insights from fluid inclusions, cathodoluminescence, and trace elements in quartz. Econ. Geol. 112, 889–918.
Martin, J.J., Armington, A.F., 1983. Effect of Growth-Rate on Quartz Defects: J. Crystal Growth 62 (1), 203–206.
Müller, A., Herrington, R., Armstrong, R., Seltmann, R., Kirwin, D.J., Stenina, N.G., Kronz, A., 2010. Trace elements and cathodoluminescence of quartz in stockwork veins of Mongolian porphyry-style deposits. Mineral. Deposita 45, 707–727.
Maydagán, L., Franchini, M., Rusk, B., Lentz, D.R., McFarlane, C., Impiccini, A., Ríos, F.J., Rey, R., 2015. Porphyry to Epithermal Transition in the Altar Cu-(Au-Mo) Deposit, Argentina, Studied by Cathodoluminescence, LA-ICP-MS, and Fluid Inclusion Analysis. Econ. Geol. 110, 889–923.
Maydagán, L., Franchini, M., Impiccini, A., Lentz, D., Patrier, P., Beaufort, D., 2018. Chlorite, white mica and clay minerals as proximity indicators to ore in the shallow porphyry environment of Quebrada de la Mina deposit, Argentina. Ore Geol. Rev. 92, 297–317.
Müller, A., Wanvik, J.E., Ihlen, P.M., 2012. Petrological and Chemical Characterisation of High-Purity Quartz Deposits with Examples from Norway. In Gotze, J., Mockel, R., ed., Quartz: Deposits, Mineralogy and Analytics, 1st edition. Springer Geology. pp. 71–118.
Müller, A., Wiedenbeck, M., van den Kerkhof, A.M., Kronz, A., Simon, K., 2003. Trace elements in quartz—a combined electron microprobe, secondary ion mass spectrometry, laser-ablation ICP-MS, and cathodoluminescence study. Eur. J. Mineral. 15, 747–763.
Mungall, J.E., 2002. Roasting the mantle: slab melting and the genesis of major Au and Au-rich Cu deposits. Geology 30, 915–918.
Munoz, J.L., 1984. F-OH and Cl-OH exchange in micas with applications to hydrothermal ore deposits. In: Bailey SW (ed), Micas. Reviews in Mineralogy Mineralogical Society of America, Washington, DC. 13, pp. 469–493.
Munoz, J.L., 1992. Calculation of HF and HCL fugacities from biotite compositions: revised equations. Geol. Soc. Am. Abstract Programs 24, A221.
Nachit, H., Ibhi, A., Abia, E.H., Ohoud, M,B., 2005. Discrimination between primary magmatic biotites, reequilibrated biotites and neoformed biotites. Comptes Rendus Geosci. 337, 1415–1420.
Ohmoto, H., Goldhaber, M.B., 1997. Sulfur and carbon isotopes. In: Barnes HL (ed) Geochemistry of hydrothermal ore deposits, 3rd edn. Wiley, New York. pp. 517–611.
Ostapenko, G.T., Tarashchan, A.N., Mitsyuk, B.M., 2007. Rutile-quartz geothermobarometer. Geochem. Int. 45 (5), 506–508.
Penniston-Dorland, S.C., 2001. Illumination of vein quartz textures in a porphyry copper ore deposit using scanned cathodoluminescence: Grasberg Igneous Complex, Irian Jaya, Indonesia. Am. Mineral. 86, 652–666.
Parry, W.T., Ballantyne, G.H., Wilson, J.C., 1978. Chemistry of biotite and apatite from a vesicular quartz latite porphyry plug at Bingham. Utah. Economic Geol. 73, 1308–1314.
Parsapoor, A., Khalili, M., Tepley, F., Maghami, M., 2015. Mineral chemistry and isotopic composition of magmatic, re-equilibrated and hydrothermal biotites from Darreh-Zar porphyry copper deposit, Kerman (Southeast of Iran). Ore Geol. Rev. 66, 200–218.
Rieder, M., 2001. Mineral nomenclature in the mica group: the promise and the reality. Eur. J. Mineral. 13, 1009–1012.
Rieder, M., Cavazzini, G., Yakonov, Y.D., Frank-Kanetskii, V.A., Gottardi, G., Guggenheim, S., Koval, P.V., Muller, G., Neiva, A.M.R., Radoslovich, E.W., Robert, J.L., Sassi, F.P., Takeda, H., Weiss, Z., Wones, D.R., 1998. Nomenclature of the micas. Can. Mineral. 36, 905–912.
Robb, L.J., 2005. Introduction to Ore-forming Processes. Blackwell, Oxford, pp. 1–373.
Rusk, B., 2012. Cathodoluminescent Textures and Trace Elements in Hydrothermal Quartz. In: Gotze, J., Mockel, R., ed., Quartz: Deposits, Mineralogy and Analytics, 1st edition: Springer Geology, pp. 307–329.
Rusk, B.G., 2006. Intensity of quartz cathodoluminescence and trace-element content in quartz from the porphyry copper deposit at Butte, Montana. Am. Mineral. 91, 1300–1312.
Rusk, B., Reed, M., 2002. Scanning electron microscope-cathodoluminescence analysis of quartz reveals complex growth histories in veins from the Butte porphyry copper deposit, Montana. Geology 30, 727–730.
Seedorff, E., Dilles, J.H., John, M., Proffett, J., Einaudi, M.T., Zurcher, L., Stavast, W.J.A., Johnson, D.A., Barton, M.D., 2005. Porphyry Deposits: Characteristics and Origin of Hypogene Features. Economic Geology 100th Anniversary Volume, 251–298.
Selby, D., Nesbitt, B.E., 2000. Chemical composition of biotite from the Casino porphyry Cu-Au-Mo mineralization, Yukon, Canada: evaluation of magmatic and hydrothermal fluid chemistry. Chem. Geol. 171, 77–93.
Sharp, D.Z., 1990. A laser-based microanalytical method for the in situ determination of

oxygen isotope ratios of silicates and oxides. Geochim. Cosmochim. Acta 54, 1353–1357.
Sharp, Z.D., Atudorei, V., Durakiewicz, T., 2001. A rapid method for determination of hydrogen and oxygen isotope ratios from water and hydrous minerals. Chem. Geol. 178, 197–210.
Sheets, R.W., Nesbitt, B., Muehlenbacks, K., 1996. Comparative geochemistry of porphyritic intrusions of the Babine Lake area, west-central BC: implications for porphyry copper exploration. Geol. Soc. Am. Abstr. 28, 93.
Shinohara, H., Hedenquist, J.W., 1997. Constraints on magma degassing beneath the Far Southeast Porphyry Cu-Au Deposit, Philippines. J. Petrol. 38, 1741–1752.
Sillitoe, R.H., 2010. Porphyry Copper Systems. Econ. Geol. 105, 3–41.
Sun, W.D., Liang, H.Y., Ling, M.X., Zhan, M.Z., Ding, X., Zhang, H., Yang, X.Y., Li, Y.L., Ireland, T.R., Wei, Q.R., Fan, W.M., 2013. The link between reduced porphyry copper deposits and oxidized magmas. Geochim. Cosmochim. Acta 103, 263–275.
Suzuoki, T., Epstein, S., 1976. Hydrogen isotope fractionation between OH-bearing minerals and water. Geochim. Cosmochim. Acta 40, 1229–1240.
Taylor, R.P., 1983. Comparison of biotite geochemistry of Bakircay, Turkey, and Los Pelambres, Chile, porphyry copper systems. Trans. Inst. Min. Metall., Sect. B 92, B16–B22.
Thomas, J.B., Watson, E.B., Spear, F.S., Shemella, P.T., Nayak, S.K., Lanzirotti, A., 2010. TitaniQ under pressure: the effect of pressure and temperature on the solubility of Ti in quartz Contrib. Mineral. Petrol. 160 (5), 743–759.
Tindle, A.G., Webb, P.C., 1990. Estimation oflithium contents in trioctahedral micas using microprobe data: application to micas from granitic rocks. Eur. J. Mineral. 2, 595–610.
Tischendorf, G., Forster, H.J., Gottesmann, B., 1999. The correlation between lithium and magnesium in trioctahedral micas: improved equation for Li_2O estimation from MgO data. Mineral. Mag. 63 (1), 57–74.
Tischendorf, G., Forster, H.J., Gottesmann, B., 2001. Minor and trace-element composition of trioctahedral micas: a review. Mineral. Mag. 65 (2), 249–276.
Tischendorf, G., Förster, H.J., Gottesmann, B., Rieder, M., 2007. True and brittle micas: composition and solid-solution series. Mineral. Mag. 71, 285–320.
Tischendorf, G., Gottesmann, B., Forster, H.J., Trumbull, R.B., 1997. On Li-bearing micas: estimating Li from electron microprobe analyses and improved diagram for graphical representation. Mineral. Mag. 61, 809–834.
Ulrich, T., Günther, D., Heinrich, C.A., 2001. The evolution of a porphyry Cu-Au deposit based on LA-ICP-MS analyses of fluid inclusions: Bajo de la Alumbrera, Argentina. Econ. Geol. 96, 1743–1774.
Wan, D.F., Fan, T.Y., Tian, S.H., 2005. The chromium analytical technique for hydrogen isotopes. Acta Geolica Sinica 26, 35–38 (in Chinese with English abstract).
Wang, F.Y., Ling, M.X., Ding, X., Hu, Y.H., Zhou, J.B., Yang, X.Y., Liang, H.Y., Fan, W.M., Sun, W.D., 2011a. Mesozoic large magmatic events and mineralization in SE China: oblique subduction of the Pacific plate. Int. Geol. Rev. 53, 704–726.
Wang, L., 2010. Metallogenic model and prospecting potential in Dabaoshan molybdenum polymetallic ore deposit, North Guangdong Province. Dissertation, China University of Geosciences (in Chinese with English abstract).
Wang, L., Hu, M., Yang, Z., Qu, W., Xia, J., Chen, K., 2011b. U-Pb and Re-Os geochronology and geodynamic setting of the Dabaoshan polymetallic deposit, northern Guangdong Province, South China. Ore Geol. Rev. 43, 40–49.
Wang, Q.Y., Hu, R.Z., Peng, J.T., Bi, X.W., Wu, L.Y., Liu, H., Su, B.X., 2007. Characteristics and significance of the fluid inclusions from Yaogangxian tungsten deposit in south of Hunan. Acta Petrologica Sinica 23 (9), 2263–2273 (in Chinese with English abstract).
Wark, D.A., Watson, E.B., 2006. TitaniQ: a titanium-in-quartz geothermometer. Contrib. Mineral. Petrol. 152(6) 743–754.
Watson, E.B., 1996. Surface enrichment and trace-element uptake during crystal growth Geochimica et Cosmochimica Acta 60 (24), 5013–5020.
Watson, E.B., 2004. A conceptual model for near-surface kinetic controls on the trace-element and stable isotope composition of abiogenic calcite crystals Geochimica et Cosmochimica Acta 68 (7), 1473–1488.
Watson, E.B., Liang, Y., 1995. A simple model for sector zoning in slowly grown crystals: implications for growth rate and lattice diffusion, with emphasis on accessory minerals in crustal rocks. Am. Mineral. 80(11–12) 1179–1187.
Wilkinson, J.J., Chang, Z., Cooke, D.R., Baker, M.J., Wilkinson, C.C., Inglis, S., Chen, H., Bruce Gemmell, J., 2015. The chlorite proximitor: a new tool for detecting porphyry ore deposits. J. Geochem. Explor. 152, 10–26.
Wones, D.R., Eugster, H.P., 1965. Stability of biotite: experiment, theory, and application. Am. Mineral. 50, 1228–1272.
Xi, B.B., Zhang, D.H., Zhou, L.M., Zhang, W.H., Wang, C., 2008. Characteristics of ore-forming fluid evolution in Dajishan tungsten deposit, Quanan County, Jiangxi. Acta Geologica Sinica 82 (7), 956–966 (in Chinese with English abstract).
Yavuz, F., 2003. Evaluating micas in petrologic and metallogenic aspect: I-definitions and structure of the computer program MICA+. Comput. Geosci. 29, 1203–1213.
Yavuz, F., Öztas, T., 1997. BIOTERM-a program for evaluating and plotting microprobe analyses of biotite from barren and mineralized magmatic suites. Comput. Geosci. 23, 897–907.
Zhang, T.F., Pan, X.F., Yang, F., Li, Y., Hu, B.G., Zhu, X.Y., Zhao, M., 2012. A study of fluid inclusions in Zhushahong copper-gold porphyry deposit, Dexing, Jiangxi. Mineral Deposits 31 (4), 861–880.
Zheng, Y.F., Chen, J.F., 2000. Stable isotope geochemistry. Science Press, Beijing, pp. 1–315 (in Chinese).
Zhong, L., Li, J., Peng, T., Xia, B., Liu, L., 2013. Zircon U-Pb geochronology and Sr-Nd-Hf isotopic compositions of the Yuanzhuding granitoid porphyry within the Shi-Hang Zone, South China: Petrogenesis and implications for Cu-Mo mineralization. Lithos 177, 402–415.
Zhong, L., Liu, L., Xia, B., Li, J., Lin, X., Xu, L., Lin, L.Z., 2010. Re-Os Geochronology of Molybdenite from Yuanzhuding Porphyry Cu-Mo Deposit in South China. Resour. Geol. 60, 389–396.
Zhou, X.M., Sun, T., Shen, W.Z., Shu, L.S., Niu, Y.L., 2006. Petrogenesis of Mesozoic granitoids and volcanic rocks in South China: a response to tectonic evolution. Episodes 29, 26–33.
Zhou, Y.Z., Zeng, C.Y., Li, H.Z., An, Y.F., Liang, J., Lü, W.C., Yang, Z.J., He, J.G., Shen, W.J., 2012. Geological evolution and oreprospecting targets in southern segment of Qinzhou Bay-Hangzhou Bay juncture orogenic belt, southern China. Geol. Bull. China 31 (2/3), 486–491 (in Chinese with English abstract).
Zhu, C., Sverjensky, D.A., 1991. Partitioning of F-Cl-OH between minerals and hydrothermal fluids. Geochim. Cosmochim. Acta 55, 1837–1858.
Zhu, C., Sverjensky, D.A., 1992. F-Cl-OH partitioning between biotite and apatite. Geochim. Cosmochim. Acta 56, 3435–3467.